

## Chapter 2

# One-Dimensional SiC Nanostructures: Synthesis and Properties

Weimin Zhou, Yafei Zhang, Xiaoming Niu, and Guoquan Min

**Abstract** SiC with unique properties, such as wide band gap, excellent thermal conductivity, chemical inertness, high electron mobility, and biocompatibility, promises well for applications in microelectronics and optoelectronics, as well as nanocomposites. The chapter reviews the recent progress on one-dimensional SiC nanostructures in both experimental and theoretical level, including synthesis methods and some properties (field emission, optical, electronic transport, mechanical, photocatalyst, and hydrogen storage) of SiC nanowires. Importantly, some novel results on SiC nanowires were elucidated clearly in our laboratory. Personal remarks end with some views on development and application of one-dimensional SiC nanostructures.

## 2.1 Introduction

Recently, one-dimensional (1D) semiconductor nanostructures (wires, rods, belts, and tubes) have become the focus of intensive research, owing to their unique application in the fabrication of electronic, optoelectronic, and sensor devices on a nanometer scale. They possess novel properties intrinsically associated with low dimensionality and size confinement, which make “bottom-up” construction of nanodevices possible [1–7]. Because of their potential applications in nanodevices, 1D semiconductor nanomaterials were selected as one of the top 10 technologies by the MIT Technical review in 2003 [8]. So far, many kinds of 1D semiconductor nanomaterials, including single element [9–14] and compound semiconductors [15–21], have been successfully synthesized by a rich variety of methods, and the detailed research information on these 1D nanostructures can be readily seen in the pertinent literature [22–44]. Among these semiconductor nanowires, SiC has very unique properties, such as wide bandgap, excellent thermal conductivity, chemical inertness, high electron mobility, and biocompatibility, which promise well for applications in microelectronics and optoelectronics, and has thus attracted much interest from the materials and devices communities [45–47]. In particular, SiC nanowires



are used for the reinforcement of various nanocomposite materials or as nanocontacts in harsh environments, mainly due to their superior mechanical properties and high electrical conductance. Hence, research on 1D SiC nanowires is highlighted, both from the fundamental research standpoint and for potential application in nano-devices and nanocomposites.

In this chapter, research on 1D SiC nanostructure (nanowires/nanotubes, nanowire heterostructures, and nanowire arrays) is highlighted in a comprehensive review and some important results of pioneering work conducted in our laboratory on SiC nanowires are reported. The review is divided into three main parts. The first part introduces crystallographic structures of SiC; the second part focuses on the synthesis of SiC nanowires and the third part on some special nanostructures of orient SiC nanowire arrays, SiC nanotubes, and SiC nanowire heterostructures. Some properties of SiC nanowires are described later. The review ends with a summary, which is our personal opinion on future research in 1D SiC nanowires.

## 2.2 Crystallographic Structures of SiC

SiC is a IV–IV compound semiconductor and occurs in many different crystal structures (polytypes). The crystalline structure of SiC can be considered to consist of the close-packed stacking of double layers of Si and C atoms. Each C or Si atom is surrounded by four Si or C atoms in strong tetrahedral  $SP^3$  bonds. The distance between neighboring Si and C atoms is approximately 3.08 Å for all polytypes [48,49]. There are more than 200 polytypes in existence. The polytypes can be defined by the number of stacking layers in a unit cell. The atom arrangements of popular polytypes are 3C, 4H, and 6H. The 3C-SiC polytype is the only cubic polytype and it has a stacking sequence ABCABC. 4H-SiC consists of an equal number of cubic and hexagonal bonds with stacking sequences of ABCB. Two-thirds of 6H-SiC is composed of cubic bonds and one-third of hexagonal bonds, with stacking sequences of ABCACB. Only 3C-SiC is referred to as  $\beta$ -SiC; other 4H- and 6H-SiC are called  $\alpha$ -SiC. Figure 2.1 shows the schematic diagram illustrating the stacking layer of

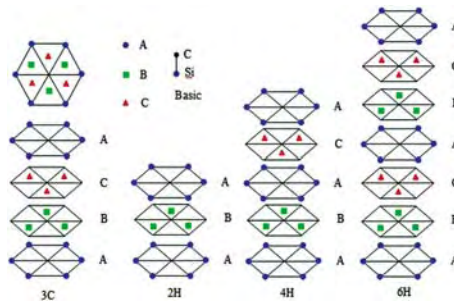


**Fig. 2.1** The stacking sequence of 3C-, 2H-, 4H-, and 6H-SiC



**Table 2.1** Typical properties of SiC and other semiconductors [49]

	Si	GaAs	3C-SiC	4H-SiC	6H-SiC	Diamond
Lattice $a$ (Å)	5.43	5.65	4.36	3.08	3.08	3.567
Lattice $a$ (Å)	5.43	5.65	4.36	15.12	10.05	3.567
Bond length (Å)	2.35	2.45	1.89	1.89	1.89	1.54
TEC ( $10^{-6}$ K)	2.6	5.73	3.0	–	4.5	0.8
Density ( $\text{g cm}^{-3}$ )	2.3	5.3	3.2	3.2	3.2	3.5
Thermal conductivity ( $\text{W cm}^{-1} \text{K}^{-1}$ )	1.5	0.5	5	5	5	2
Melting point ( $^{\circ}\text{C}$ )	1,420	1,240	2,830	2,830	2,830	4,000
Mohs hardness			9	9	9	10
$E_g$ (eV)	1.1	1.43	2.3	3.3	3.0	5.4

the common 3C-, 2H-, 4H-, and 6H-SiC. In general,  $\beta$ -SiC, which often appears at low temperature, is easy to nucleate and grow. However, 4H-SiC and 6H-SiC are known as high-temperature stable polytypes, which need relatively high temperatures to grow. Typical properties of SiC and other semiconductors are summarized in Table 2.1.

SiC materials are extremely hard, very inert, and have high thermal conductivity. Properties such as the breakdown electric field strength, the saturated drift velocity, and the impurity ionization energies are unique for the different polytypes.  $\beta$ -SiC possesses the smallest bandgap ( $\sim 2.4$  eV) and has the highest electron carrier mobility compared with  $\alpha$ -SiC, which makes it an important SiC material in the microelectronics industry [50]. Because of these excellent properties, SiC is a perfect material in the electronics industry, with a wide application in the areas of high-temperature device, high-power device, high-frequency device, and optoelectronic device, including rectifiers, power switches, RF, and microwave power devices [51, 52]. Besides, SiC, known for its high-temperature structure and reinforced composite material, can be also find application in the aerospace, car, machine, and petrochemical industries [52–57].

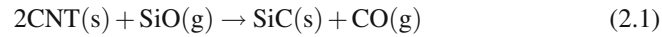
## 2.3 Synthesis of One-Dimensional SiC Nanostructures

Since the discovery of the carbon nanotube (CNT) [58, 59], 1D SiC nanostructures have attracted many scientists because of their unique electronic, optical, and mechanical properties. A significant progress in synthesis methods in SiC nanowire/nanotube was achieved by various technologies, such as carbon template, arc discharge, chemical vapor deposition (CVD) via silicon precursor, carbothermal reduction of silica xerogels, etc. In this section, some recent progress in the fabrication of 1D SiC nanostructures is addressed.



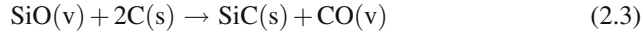
### 2.3.1 Carbon Nanotube-Confined Reaction

In 1994, Prof. Zhou at the University of Arizona reported for the first time a method to produce SiC whiskers without the presence of metal catalysts by reacting carbon nanotubes with SiO at 1,700°C under a flow of Ar [60]. The length and diameter of the as-synthesized SiC nanowire are one order greater in magnitude than that of the carbon nanotube precursor. The dark carbon nanotubes with hollow cores are converted to solid greenish SiC nanowires. The carbon nanotube acts as a template and defines the diameter and length of SiC nanowires. The reaction is as follows:



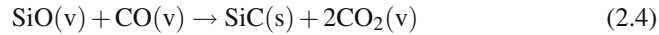
In 1995, Lieber's group [61] at Harvard University reported in *Nature* that carbon nanotubes can be converted to carbide rods by reaction with SiO or Si-I<sub>2</sub>. The SiC nanorods (NRs) are in high yield with typical diameters similar to or much smaller than the diameters of the carbon nanotube, of between 2 and 30 nm and lengths of up to 20 μm.

A two-step reaction process has been developed to synthesize SiC nanorods at 1,400°C [62]. SiO vapor was generated via the silicon reduction of silica, and reacted with the carbon nanotube to form SiC nanorods. In the two-step reaction process, the reaction equations are

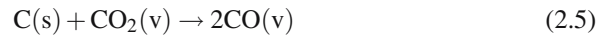


The nanorods are single-crystalline β-SiC with the diameters between 3 and 40 nm. The thinner SiC nanorods, namely 3 nm in diameter, show a high density of defect planes on the (111) basal planes. In this experiment, the diameter of the SiC nanowire differed from the precursor carbon nanotube. It may be explained as follows.

The generated CO vapor in (3) can react with SiO vapor on the generated SiC nanorod surface by the following reaction:



In this reaction, the diameter of the synthesized SiC nanorods is larger than that of the starting carbon nanotubes. On the contrary, the thinner diameters of SiC nanorods can be explained by the following reaction.



The surface of the carbon nanotubes is consumed by the CO<sub>2</sub> and the residual carbon nanotube reaction with SiO leads to thinner SiC nanorods.

The diameter and shape of the produced SiC nanorods can be controlled by the local partial pressure of CO gas and the reaction temperature, respectively. Tang



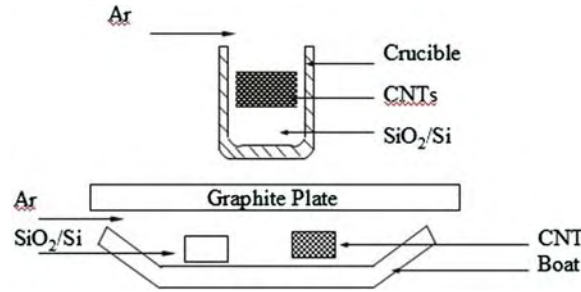


**Fig. 2.2** Geometry of the reactor. (a) Reactants of SiO<sub>2</sub>/Si source covered with carbon nanotubes were put in a crucible. (b) SiO<sub>2</sub>/Si source and carbon nanotubes were put in a boat and the latter kept clear of the former along the downstream direction of gas flowing

et al. [63] developed a new way as shown in Fig. 2.2. The generated CO byproduct from (3) can be effectively carried away from the reaction area, thus preventing reactions (4) and (5). The size of the diameter of SiC nanowires is consistent with the starting carbon nanotubes. The growth mechanism of SiC nanorods is basically a shape memory synthesis, where the product keeps the shape of the starting nanotubes to form nanorods. The shape memory synthesis has the advantages of the shape of the generated nanorods adjusted by the initial carbon nanotubes, the CO-generated concentration, and reaction temperature.

The unexpected synthesis of SiC nanorods with thermally annealing single-walled carbon nanotube sheets (SWNTs) formed by a filtration process using surfactant-dispersed nanotubes, at a significantly lower temperature of 1,000°C between two silicon wafers [64]. In the experiment, the exterior layers of the carbon nanotube sheets were converted into a network of SiC nanorods, while the carbon nanotubes interior to the sheet remained unchanged. The SEM images are shown in Fig. 2.3.

### 2.3.2 Arc Discharge

Since carbon nanotubes were synthesized by arc discharge, scientists attempted to fabricate SiC nanowires with the arc-discharge process, considering the simple setup, ease of operation and high production. Seeger et al. [65] reported for the first time the synthesis of nanometer-sized SiC whiskers using the arc-discharge process. The samples were synthesized using an arc discharge between two graphite electrodes, the anode of which was filled with a mixture SiO<sub>2</sub> and C powder in the atomic ratio 1:1. The arc discharge was ignited by 40 A at 22 V under a 53 kPa helium atmosphere. The graphite cathode of 10 mm diameter was placed horizontally, facing the composite anode of 6.15 mm diameter, which had a 3.2 mm diameter hole drilled, with 25 mm filled with a mixture of graphite and Si powder. β-SiC whiskers of 10 nm in diameter were synthesized directly.



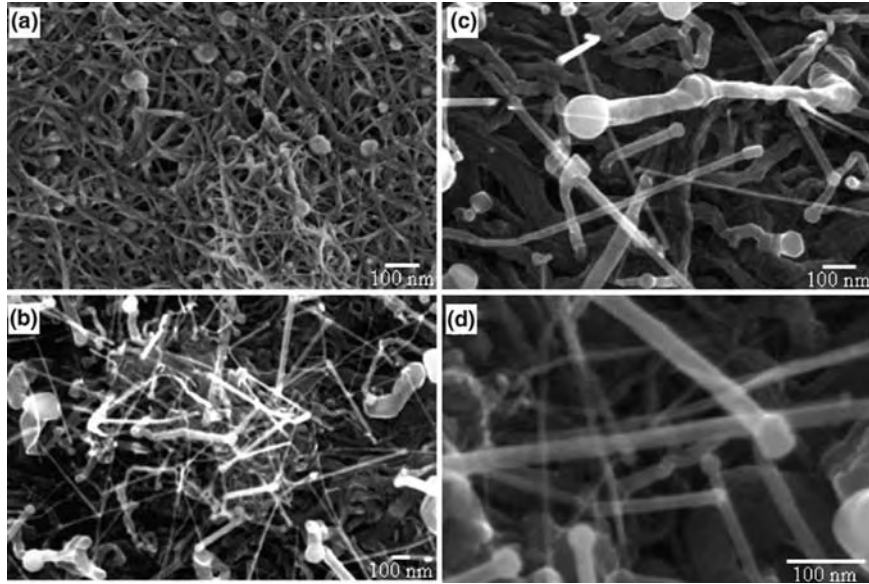


**Fig. 2.3** SEM micrographs of a carbon nanotube sheet before (a) and SiC nanorods: after (b)–(d) thermal annealing this sheet at 1,000°C between two parallel silicon wafers. The large quasi-spherical particles in (a), with a diameter of typically above 30 nm, contain iron [Ref. 3]

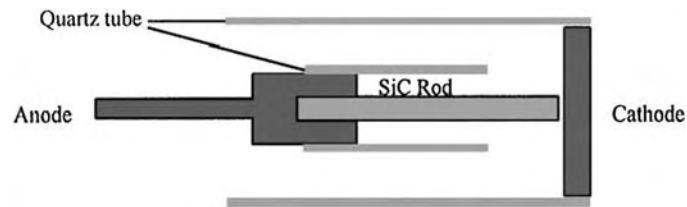


**Fig. 2.4** Arc-discharge setup

Later, Xie's group [66] devised a new route, using a SiC rod as the anode in an arc-discharge process, developed to fabricate SiC nanorods on a large scale as shown Fig. 2.4. A graphite rod (15 mm in diameter) had a hole drilled (7.5 mm in diameter and 10 mm in depth) at one end and its other end was thinned to 6 mm in diameter. A SiC rod (about 7.5 mm in diameter and 8 cm in length) was inserted into the hole and acted as the anode, and a graphite plate (with a diameter of 30 mm) was used as the cathode. The characterization indicated that the prepared nanorods possess a  $\beta$ -SiC crystal core with a uniform diameter of 5–20 nm and an amorphous SiO<sub>2</sub> wrapping layer tens of nanometers in thickness, and their lengths ranging from hundreds of nanometers to several micrometers (Fig. 2.5). A possible growth mechanism could be explained as follows: during discharging, SiC at the tip of the anode decomposes into silicon and carbon due to the high temperature of the arc-zone.



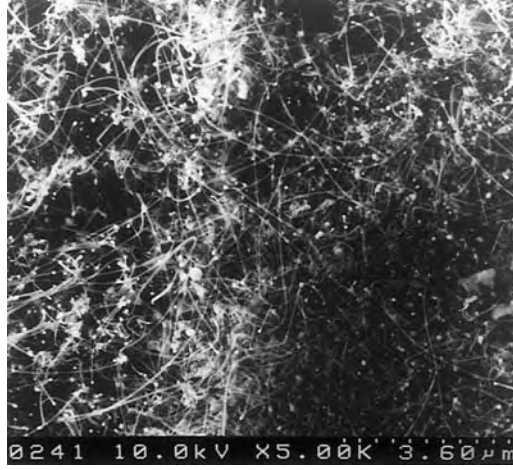
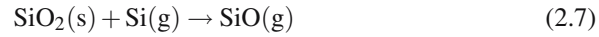


**Fig. 2.5** SEM image of the powder by arc discharge [Ref. 51]



The silicon gas may react with the quartz ( $\text{SiO}_2$ ) to form SiO gas.



Hence, the Si, C, and SiO gas were absorbed and dissolved in the liquid-iron droplets to form a liquid Fe–Si–C–O alloy. When cooled, the liquid droplets were supersaturated and the  $\beta$ -SiC core together with the  $\text{SiO}_2$  sheath was nucleated.

### 2.3.3 Laser Ablation

Laser ablation has been widely synthesized for carbon nanotubes [67, 68] and Si nanowires [69, 70], because the method can produce free-standing nanoscale material in high-purity yields at a low working temperature for high-melting and multi-component materials. Shi et al. [71] used the laser-ablation technique (Fig. 2.6) to synthesise SiC nanowires from a target of SiC target ( $25 \times 25 \times 5 \text{ mm}$ ). The KrF excimer pulsed laser beam (wavelength 248 nm, energy 400 mJ per pulse, and frequency 10 Hz) was focused on the SiC target and the ablation lasted for 2 h. Large quantities of straight, curved, and randomly oriented nanowires were formed on the graphite substrate in the system. The lengths of the nanowires were up to tens of micrometers (Fig. 2.7). There were also some spherical nanoparticles at the tips of the nanowires (as seen in Fig. 2.7). The SiC nanowire consists of a crystal SiC core with numerous stacking faults and an amorphous silicon oxide shell. The transmission electron microscopy (TEM) observation showed that the diameters of the crystalline cores varied from 20 to 70 nm and the mean value was  $\sim 55 \text{ nm}$ . The thickness of the amorphous outer layers varied from 11 to 30 nm and the mean value was  $\sim 17 \text{ nm}$ .



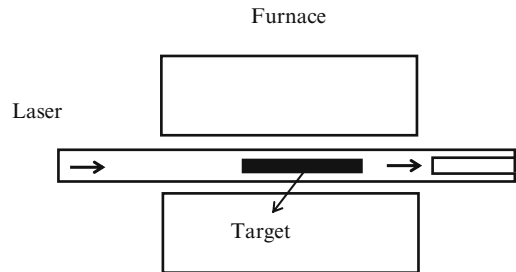


**Fig. 2.6** Laser-ablation scheme

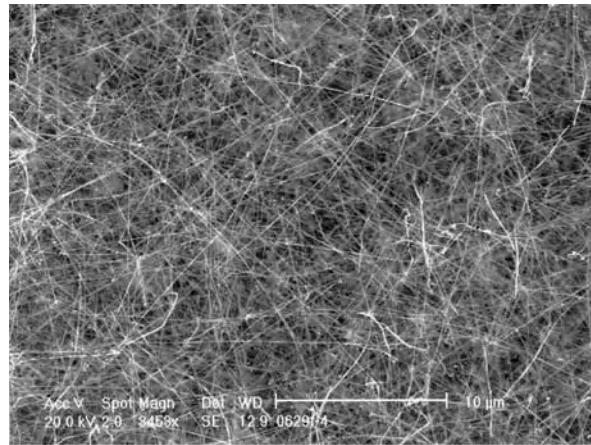


**Fig. 2.7** Typical SEM image of SiC nanowires [Ref. 71]

### 2.3.4 Sol-Gel and Carbothermal Reduction

Meng et al. [72, 73] have successfully developed a novel method to synthesize bulk quantities of  $\beta$ -SiC nanowires from silica xerogels containing carbon nanoparticles. Nanowires were fabricated by carbothermal reduction at  $1,650^{\circ}\text{C}$  for 1.5 h, followed by annealing to  $1,800^{\circ}\text{C}$  and holding for 30 min in flowing Ar atmosphere. TEM, SAED, and EDX showed that the nanowires consist of 10–25 nm diameter crystalline  $\beta$ -SiC cores surrounded by amorphous  $\text{SiO}_2$  sheathes with outer diameters between 20 and 70 nm. The nanowires formed by carbothermal reduction at  $1,650^{\circ}\text{C}$  for 2.5 h in flowing argon atmosphere are bare SiC nanowires with diameters in the range of 15–30 nm.

Silicon carbide nanorods were synthesized by sol-gel and carbothermal reduction processing with TEOS (tetraethoxysilane) and PVP (polyvinyl pyrrolidone) as starting materials and  $\text{Fe}(\text{NO}_3)_3$  as catalyst [74]. Results show that the morphologies of



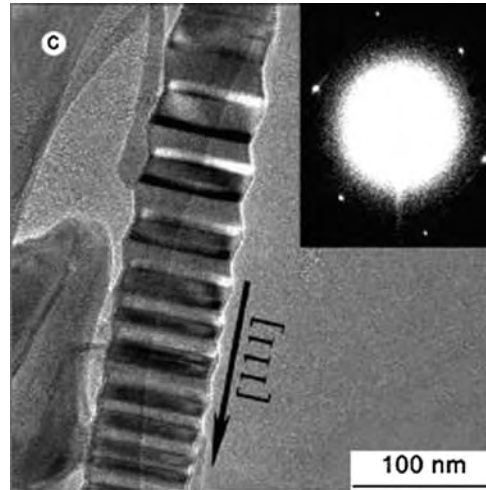


**Fig. 2.8** TEM images of resulting SiC sample catalyzed by Fe [Ref. 74]

the resulting sample are tower-like  $\beta$ -SiC nanorods which typically have a tower base width between 80 and 100 nm, a step layer thickness of about 10 nm between two layers and a height from 0.4 to 1.0  $\mu\text{m}$  (Fig. 2.8).

### 2.3.5 Chemical Vapor Deposition

In this process, a mixture of silicon (carbon) precursor of  $\text{SiH}_4$  ( $\text{SiCl}_4$ ,  $\text{Si}(\text{CH}_3)\text{Cl}$ ,  $\text{CH}_3\text{SiCl}_3$ ,  $\text{CH}_4$ ) is introduced into the reaction chamber [75–77]. During the reaction, SiC nanowires are formed on the substrate by the reaction of carbon and silicon. Although this is at the cost of lower yield, the catalyst can be deposited on the desired location of substrate, which allows for the formation of novel nanostructures by predefined position of catalyst [78].

Zhang et al. [79] used microwave plasma CVD to synthesize bulk quantity single-crystalline  $\beta$ -SiC nanowires on a Si substrate. The process is divided into two steps: first, smooth Si(100) substrates of  $10 \times 20 \times 0.6 \text{ mm}$  were ultrasonically cleaned in ethanol and etched with 3% HF acid in water for 3 min. An Fe film of a different thickness (9–105 nm) was deposited on the Si(100) substrate by the sputtering method. Then the Si substrate was placed in the CVD system. A 100 sccm hydrogen ( $\text{H}_2$ ) and a  $\sim 0.05$  sccm methane ( $\text{CH}_4$ ) were introduced into the chamber. The Si substrate temperature is from 800 to 1,000°C. Figure 2.9 shows the TEM images of the as-synthesized SiC nanowires by the CVD method. The SiC nanowires are smooth and straight. Many nanowires are cylinder shaped with a circular cross section, while some of the nanowires have cross-sectional shapes of squares, rectangles, triangles, and hexagons. Moreover, no Fe catalyst has been found on the nanowires.



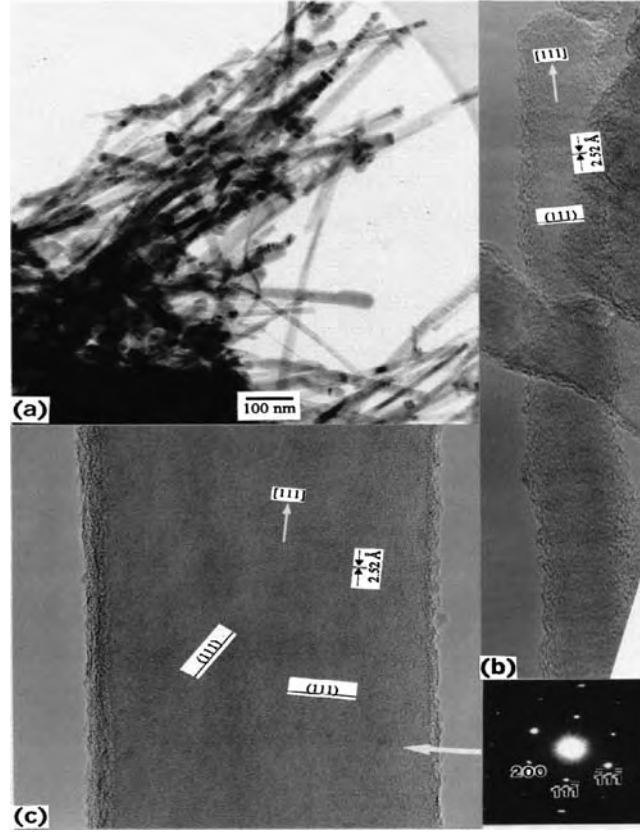


**Fig. 2.9** (a) TEM image of the nanowhiskers obtained by scratching the nanowhiskers from the Si substrate. The whiskers with circular, square, rectangle, triangle, and hexagon cross-sectional shapes. (b) High-resolution TEM image of a thin 3C-SiC nanowhisker with an approximate axial orientation of [111]. (c) A thick 3C-SiC nanowhisker with its selected area electron diffraction pattern taken by the electron beam parallel to the [011] zone axis

The most commonly occurring diameter of the nanowire sample fabricated at different temperatures and different Fe film thickness is shown in Fig. 2.10.

The relation between PL peak energy and SiC nanowire diameter is shown in Fig. 2.11. A blueshift of the PL with decreasing nanowire diameters can easily be seen for quantum confinement effects. The experimental data was made to coincide with the PL peak energy formula:  $E_{\text{peak}} = 2.16 + 32d_{\text{mo}}^{-2}$ , where  $d_{\text{mo}}$  is the most commonly occurring diameter of the  $\beta$ -SiC nanowires in the sample.

Zhou et al. [80] synthesized SiC nanorods on silicon substrate by hot filament CVD. The carbon and silicon powders in a molar ratio of 1:1 were mixed and pressed into a solid disk and loaded into a HFCVD chamber. Hydrogen fed into the chamber etched the Si/C solid disk and brought Si/C-containing reactive species to the substrate surface. After 2 h, nanowires of SiC with a 10–30 nm diameter core-shell structure were found deposited directly on the substrate surface.



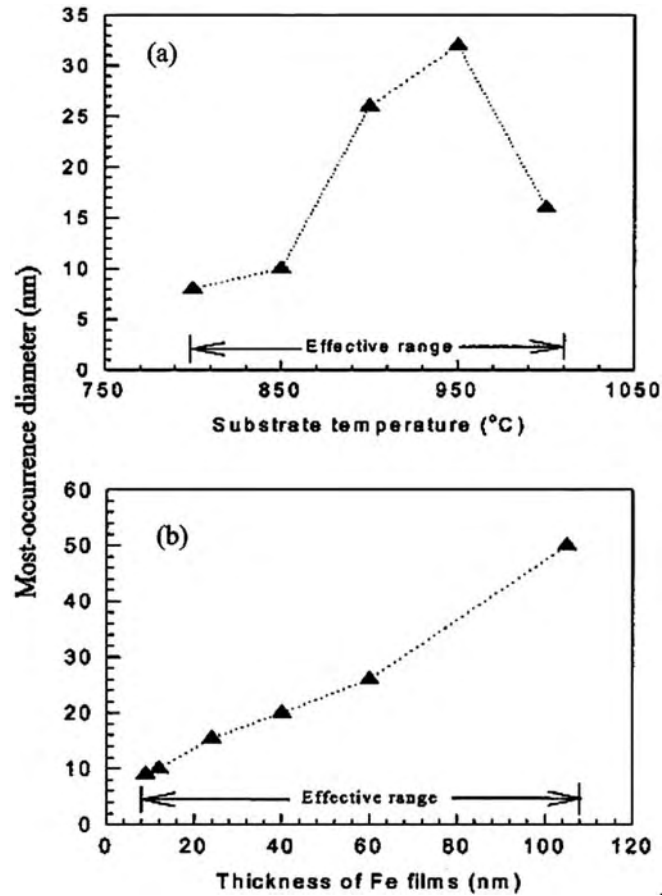


**Fig. 2.10** The dependence of the most commonly occurring diameter of the nanowhisker samples synthesized on (a) different temperatures and (b) different Fe film thickness

SiC nanowires with diameters of  $<50\text{nm}$  and lengths of several micrometers have been fabricated on Si substrates coated with a thickness of  $2\text{nm}$  Ni film by direct current magnetron sputtering methods [81]. Methyltrichlorosilane (MTS,  $\text{CH}_3\text{SiCl}_3$ ) was used as a source precursor because it has an equivalent ratio of Si to C and decomposes at a low temperature.  $\text{H}_2$  was used both as the carrier gas, which transfers the source precursor through a bubbler to the quartz reactor, and as a diluent gas, which regulates the concentration of the mixture containing MTS vapor and carrier gas. The XRD, TEM, and HRTEM observations confirm that the nanowires are single-crystalline cubic zinc-blend structures with a  $\langle 111 \rangle$  direction and SiC nanowire growth via the VLS mechanism. Figure 2.12 shows that the SiC nanowires grow under a reactor pressure of ca. 5 Torr for 2 h. The nanowires have diameters from several tens to hundreds of nanometers and are vertically well aligned without templates such as anodic alumina templates. Interestingly, Al-doped SiC



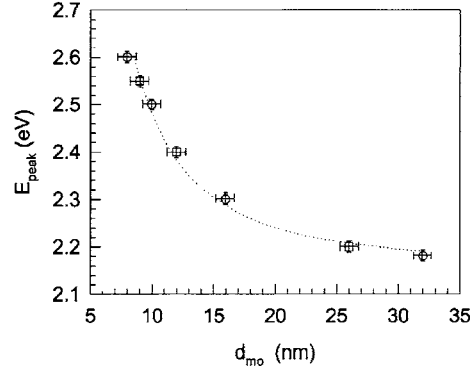


**Fig. 2.11** The dependence of the photoluminescence peak energy ( $E_{peak}$ ) on the most commonly occurring diameter ( $d_{mo}$ ) of the 3C-SiC nanowhisker samples. The *dotted line* corresponds to  $E_{peak} = 2.16 + 32d_{mo}^{-2}$ . The photoluminescence spectra were measured by using a Renishaw 2000 micro-Raman spectrometer with a 350 nm cutoff filter. The wavelength-dependent sensitivity of the optical system was calibrated by a standard lamp. The 325 nm emission line from a He-Cd laser was used to excite the luminescence

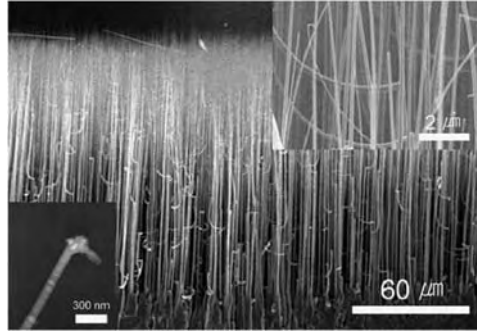


**Fig. 2.12** SEM images of vertically aligned SiCNWs grown on a Si substrate at 1,100°C for 2 h under total reactor pressure of 5 Torr. The total hydrogen flow rate including carrier and dilute gas was maintained at 775 cm<sup>3</sup> min<sup>-1</sup>. *Left lower inset* is a TEM image of SiCNWs [Ref. 81]

nanowires were fabricated for the first time by simply placing the  $AlCl_3$  precursor located upstream in the distance of 5 cm from the substrate. So, the n-type  $\beta$ -SiC nanowires can be adjusted to p- $\beta$ -SiC by doping. Figure 2.13 shows the SEM and EDS images of Al-doped SiC nanowires. An energy dispersion spectroscopy (EDS) analysis of individual SiC nanowires indicated the existence of Al in the nanowires.

SiC nanostructures in the shape of crystalline nanowire flowers have been synthesized by CVD [82]. The silicon substrate and GaN powder are placed in an alumina boat in a tube furnace. A steady flow of 300–400 sccm methane gas was introduced at 1,100°C. Flower-like structures of diameter 1–2  $\mu$ m and length 3–5  $\mu$ m are shown in Fig. 2.14a, b. A typical flower (Fig. 2.14c, d) is composed of an intertwined/weaved stem, a bulbous head consisting of a tight bundle of nanowires of



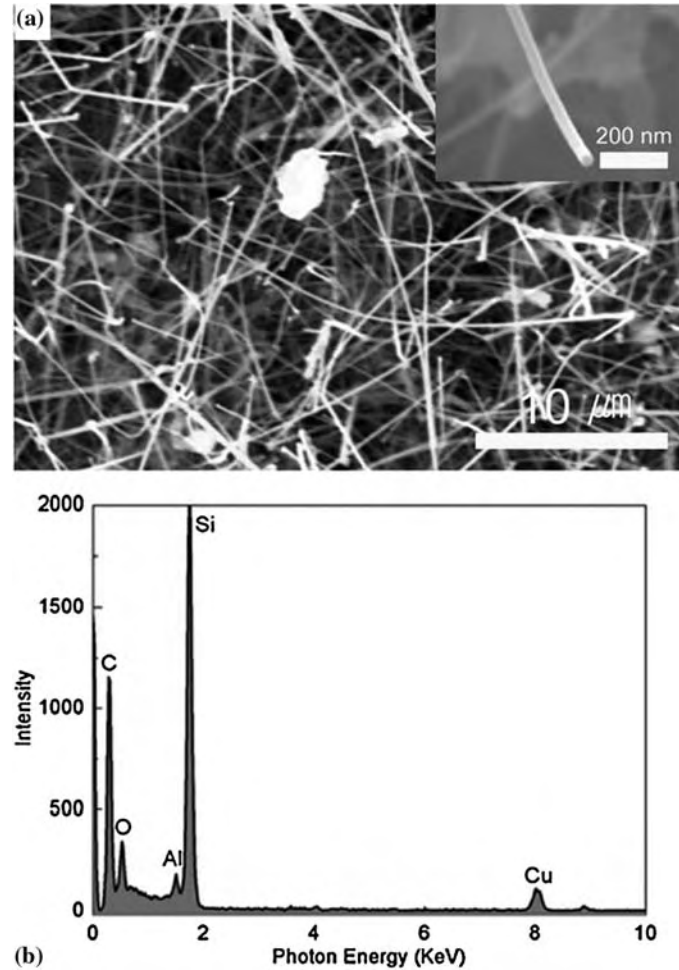


**Fig. 2.13** (a) SEM image of the NWs grown at 950°C for 5 min by using  $\text{AlCl}_3$  powders as doping precursor in  $\text{MTS-H}_2$  system under atmospheric pressure. *Inset* is TEM image of individual NW. (b) EDS data recorded from individual NW indicate the existence of Al in the NW [Ref. 81]

diameter  $\sim 100\text{--}200\text{ nm}$ , and a single catalyst particle attached at the top end of the nanowire flowers. The cross section of the broken base (Fig. 2.14c, inset) reveals a hollow stem of  $\sim 400\text{--}800\text{ nm}$  in diameter. The flowers are composed of  $\beta\text{-SiC}$  and the formation mechanism is the VLS process.

Novel 2D semiconductor SiC nanonetworks have been synthesized at relatively low temperature ( $1,250^\circ\text{C}$ ) via CVD [83]. The mixture of Si and  $\text{SiO}_2$  powders and  $\text{C}_3\text{H}_6$  were used as precursor materials. The straight or curved SiC networks that the nanowires are connected to were formed on carbon cloth. The nanowires with diameter of about  $20\text{--}70\text{ nm}$  are single-crystalline  $\beta\text{-SiC}$  and the growth direction is along [111].



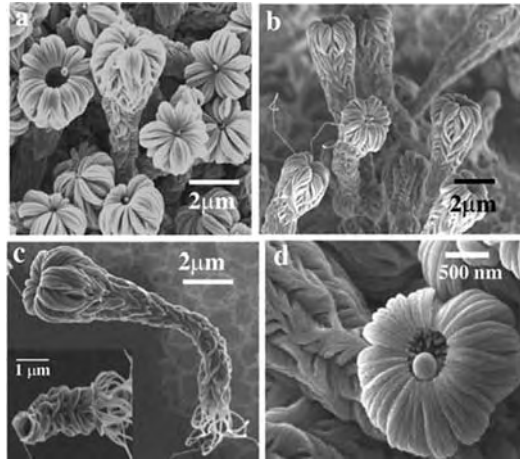


**Fig. 2.14** (a) SEM images of, and (b) an overview of, nanowire flowers grown on the silicon substrate; (c) a detached flower showing its base made up of bundles of nanowires (*inset*: cross-sectional view of a broken SiC nanowire flower); (d) a typical flower with a catalyst particle attached to the tip [Ref. 82]

SiC nanorods have been synthesized by floating catalyst methods. Iron particle catalyst was decomposed from ferrocene vapor while being carried into the chamber by the flowing gases. In the  $\text{SiCl}_4\text{--C}_6\text{H}_6\text{--H}_2\text{--Ar}$  system,  $\text{SiCl}_4$  and  $\text{C}_6\text{H}_6$  reacted with each other, catalyzed by the Fe cluster [84].

### 2.3.6 High-Frequency Induction Heating

Zhou [85] invented a novel method to fabricate  $\beta\text{-SiC}$  nanowires without catalyst introduction in high yields on the surface of the activated carbon fibers (ACFs). The experiments were performed in a vertically set high-frequency induction-heating furnace as schematically outlined in Fig. 2.15, which consisted of a quartz tube and an inductive heat cylinder of graphite coated by a layer of ACFs. First, 2 g of commercial  $\text{SiO}$  powder (purity more than 99.9%) was put into a graphite crucible. Before heating, the chamber was flushed with high-purity 100 sccm Ar to eliminate  $\text{O}_2$  by means of rotary vacuum pump for three times. Afterwards, the furnace was rapidly heated from room temperature to around  $1,450^\circ\text{C}$  within 2 min and maintained for reaction for 15 min under a total pressure of 50–100 Torr. After the furnace was cooled to room temperature in the flowing Ar, the ACF surface was deposited with a thick layer of light-blue fluff-like products having a thickness of several millimeters as shown in the inset of Fig. 2.16. Many mushroom-like lumps grew perpendicularly and separately from the surface of the ACF and joined each other at their tip.



**Fig. 2.15** High-frequency induction-heating furnace

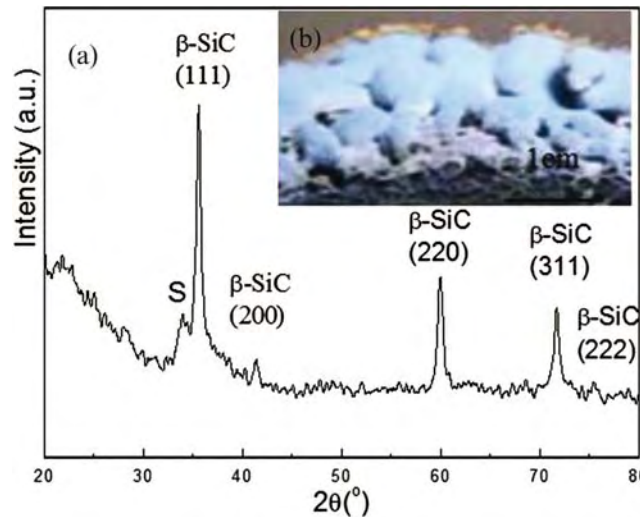
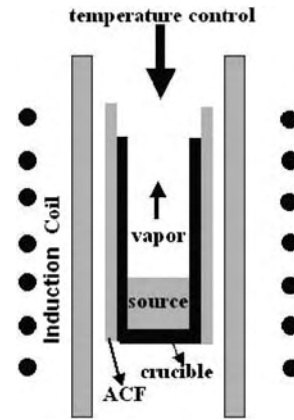


**Fig. 2.16** (a) XRD pattern of the as-synthesized products. *Inset* (b): the digital camera photo of the products

The X-ray diffraction (XRD) pattern (Fig. 2.16) suggests that the as-synthesized product consists of the crystalline zinc-blend (cubic) form of  $\beta$ -SiC with the unit constant of  $a = 4.358 \text{ \AA}$ , close to the standard value for  $\beta$ -SiC ( $4.359 \text{ \AA}$ , JCPDS card no. 29-1129). A broad peak at  $2\theta = \sim 20^\circ - 30^\circ$  may be attributed to some amorphous materials with the product. Besides, there is a low-intensity peak (marked with S) at a lower diffraction angle than that of the strong (111) peak, which usually ascribes to the stacking faults in the (111) plane. The low-magnification SEM image shown in Fig. 2.17a reveals that the product consists of numerous wire-like nanostructures (a large amount of straight, curved, randomly oriented, and free-standing nanowires) with a length of up to tens of micron. Figure 2.17b shows the chemical composition of the nanowires characterized by EDS. It is found that the nanowires are mainly



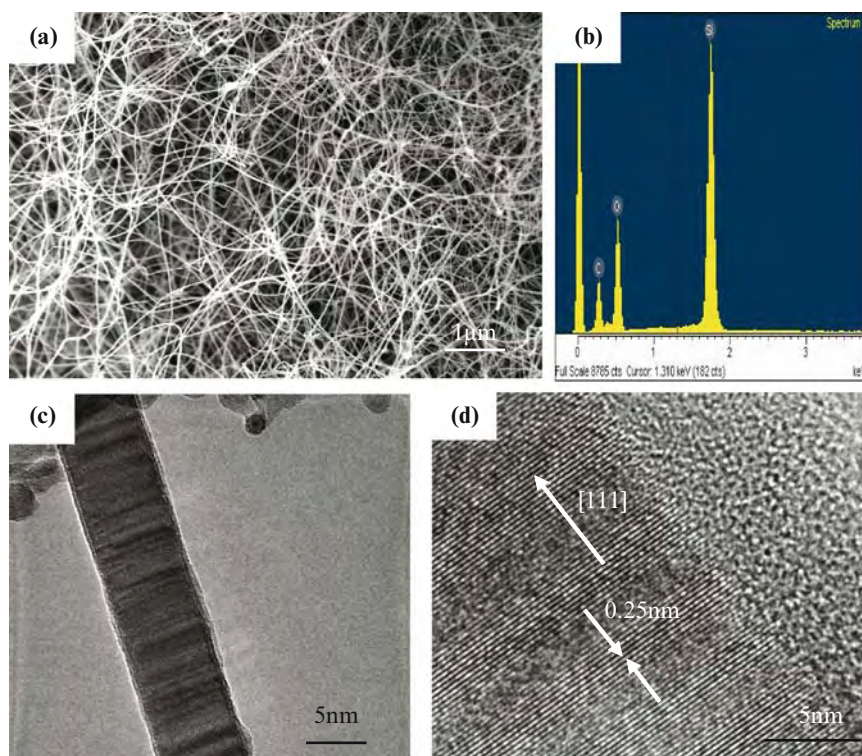


**Fig. 2.17** (a) SEM image of as-prepared samples grown at 1,450°C for 20 min by SiO powder and carbon fiber, (b) EDS spectrum of the nanowires, (c) TEM image of SiC nanowire, and (d) HRTEM image of the individual SiC nanowire

composed of Si, C, and O. The large resolution TEM image shows that a d-spacing of 0.25 nm corresponds to the (111) plane spacing, indicating that SiC nanowire grows along [111] direction.

In addition, the SiC/SiO<sub>2</sub> nanosprings, as shown in Fig. 2.18, were synthesized by the method [86]. The diameter of the nanospring is ~25 nm and with the nanospring pitch of 10 nm, this amounts to a diameter/pitch ratio of 2.5. The total nanostructures consist of three segments: two end of the nanostructure is SiC/SiO<sub>2</sub> nanocables, but SiC/SiO<sub>2</sub> nanospring is clearly seen in the midst of the whole nanostructure. TEM dark images (Fig. 2.18b) indicate that the nanospring is composed of a crystalline core and an amorphous coating. In the previous chapter, the important role of the catalyst in the formation of SiC/SiO<sub>2</sub> nanosprings was elucidated by Zhang et al. [87], which is different from our experiment without a catalyst. The helical spring structure is the most fundamental structural configuration for DNA and many biological proteins, which is due to van der Waals force and hydrogen bonding [88]. These shapes of nanostructures will be found to be a great potential application in electronic circuits and light-emitting devices such as nanospring-based transducers and actuators, and tunable functional components



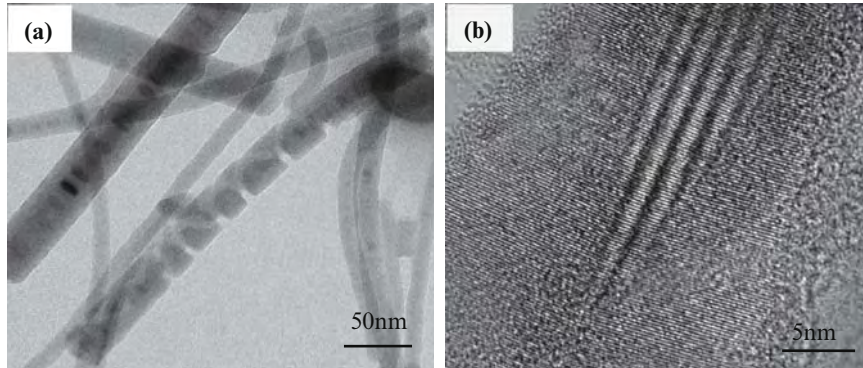


**Fig. 2.18** (a) Typical TEM images for SiC/SiO<sub>2</sub> nanosprings and (b) HRTEM image nanostructures

for MEMS and NEMS. Moreover, the nanosprings are preferable to 1D and 0D nanostructures when acting as reinforcements in advanced materials because of their better-combined interface between SiC nanosprings and the matrix in the same condition.

Similarly, Shen et al. [89] used high-frequency induction heating to synthesize bamboo-like  $\beta$ -SiC nanowires by thermal evaporation of SiO + C + GaN powders in an Ar atmosphere at 1,350°C for 1h. Later, they adjusted the mixture ratio of SiO + C + GaN powders. Hierarchical single-crystalline  $\beta$ -SiC nanowires have been successfully synthesized. Studies found that the central nanowires have diameters of  $\sim 10$ – $20$  nm and the branched nanoplatelets have thicknesses of 5–10 nm [90].

### 2.3.7 Comparison of Methods of SiC Nanowire Synthesis

The aforementioned methods to synthesize SiC nanowire – namely carbon nanotube template, arc discharge, CVD via silicon and carbon precursor – and the high-frequency heating method invited by us, have been often reported during the last several years. To show the difference clearly, Table 2.2 provides the comparison of several methods of synthesizing SiC nanowire. In most cases the product is available at the cost of either high-purity or expensive CNT or the hazardous and easily explosive silicon (carbon) precursor of SiH<sub>4</sub> or SiCl<sub>4</sub>(CH<sub>4</sub>). In addition, the synthesized materials were low in yield and purity and the methods time-consuming. Hence, the preparation of pure SiC on a large scale is still a challenge. Fortunately, we have developed a method for low-cost, large-scale production of  $\beta$ -SiC nanowires by high-frequency heating of SiO powders and ACF layers. The synthesized, high yield, SiC nanowires were directly deposited on ACF without metal catalyst introduction. Most importantly, the ACF and SiO powders are readily available because they are mass-produced in the industry and the technology of SiC nanowire synthesis invented by us can easily be scaled up to industrial levels.



**Table 2.2** The comparison of several synthetic methods of SiC nanowire

Synthesized methods	Efficiency	Cost	Temperature (°C)	Diameter (nm)	Catalyst
Carbon nanotube-confined reaction	Low	Higher	1,400	20–25	No
Arc discharge	Higher	Low	3,000	20–60	Yes
Laser ablation	High	High		20–70	Yes
Sol-gel and carbothermal reduction	Higher	Lower	900	40–80	No
Chemical vapor deposition method	Higher	Higher	1,100	10–100	Yes
High-frequency induction heating	Higher	Lower	1,450	5–20	No

## 2.4 Orient SiC Nanowire Arrays

With the development of electronic and photonic devices such as light-emitting diodes and laser diodes, field-emission display, high density and well-aligned nanowire arrays would be necessary. The unique structure and features of the anodic alumina membranes (AAM) make it an ideal template for the synthesis of aligned nanostructures. Li et al. [91] reported for the first time the synthesis of large-area, highly oriented, SiC nanowire arrays in an ordered nanoporous AAO template through a chemical vapor reaction method. The 1.2:1 molar mixture of ball-milled Si and SiO<sub>2</sub> and AAO template were placed in a graphite cell. The C<sub>3</sub>H<sub>6</sub> flow of 8–10 sccm was introduced from the bottom of the graphite cell and maintained for 3–5 min at 1,230°C under a total gas pressure of 540–650 Torr. The results show that the SiC nanowires are single crystalline with diameters of ~30–60 nm and lengths of ~8 μm, which are parallel to each other, uniformly distributed, highly aligned, and in agreement with the nanopore diameter of the AAO template. The fabricated SiC nanowires grow along the [111] direction and possess a high density of planar defect.

Aligned SiC nanowires have also been synthesized by reaction-aligned carbon nanotubes with SiO [92]. High-magnification SEM observations (Fig. 2.19) show that the products consist of highly oriented nanowires that are similar in appearance to the originally aligned carbon nanotubes. The SiC nanowires within the arrays have diameters (10–40 nm), spacing (~100 nm), and length (up to 2 mm) similar to those of the aligned carbon nanotubes. The SiC nanowire is a solid rod and does not have a hollow core structure (Fig. 2.20). The periphery of the SiC nanowire is very clean, without any coating of amorphous material, and possesses a high density of planar defects or stacking faults, which are perpendicular to the wire axes. The selected area electron diffraction (SAED) pattern (inset of Fig. 2.20a) demonstrates that the SiC nanowire has a single-crystalline phase.

Highly aligned β-SiC nanowires with a mean diameter of 40 nm and length of 500 μm on a large area Si substrate were synthesized by a novel catalytic reaction



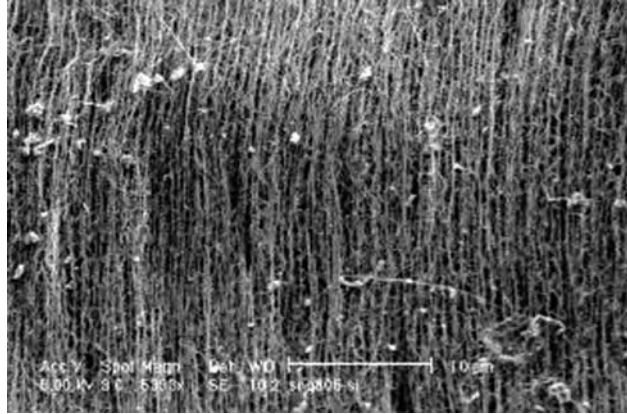


**Fig. 2.19** High-magnification SEM image of a SiC nanowire array, showing that the wires are highly aligned and have uniform external diameters and spacing between wires. The particles present on the array surface are silicon-containing particles formed and deposited during reaction [Ref. 92]

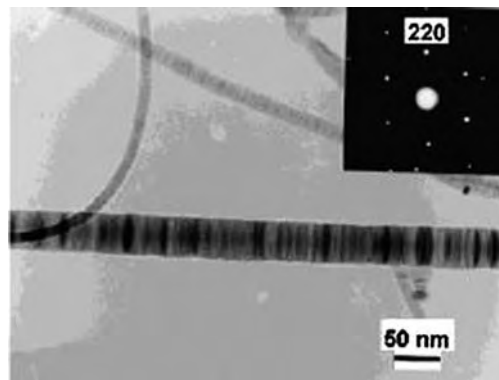


**Fig. 2.20** TEM image of  $\beta$ -SiC nanowires. The SiC nanowires exhibit a high density of stacking faults perpendicular to the wire axes. The *inset* shows a selected area electron diffraction pattern of the  $\beta$ -SiC nanowires [Ref. 20]

1,100°C [93]. The Si substrate and  $\text{CH}_4$  were used as the Si and C source, respectively. The Si substrate was coated with Ga metal, GaN powder, and Fe nanoparticle catalyst.

## 2.5 SiC Nanotubes

Sun et al. [94] used the equipment (Fig. 2.21) to synthesise SiC nanotubes (SiCNTs).  $\text{SiO}$  powders were placed at position A, the middle of the high-temperature zone of the furnace. Four pieces of Si substrate on which multiwalled carbon nanotube



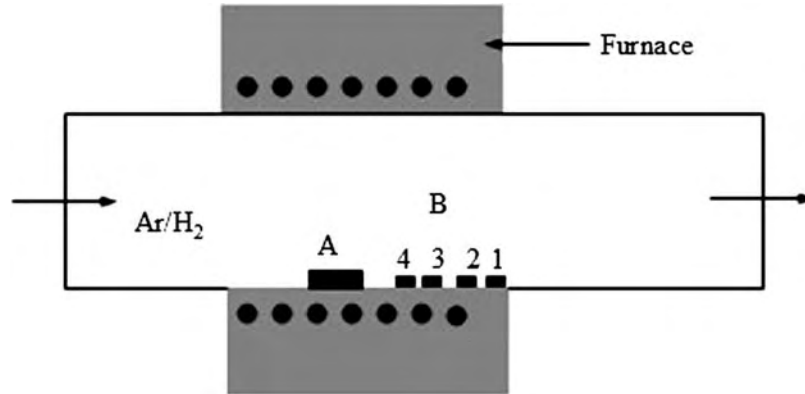


**Fig. 2.21** Synthesis apparatus

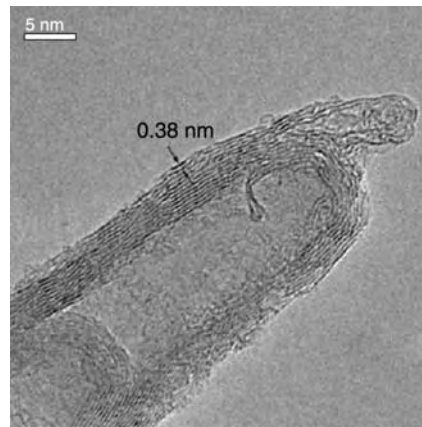


**Fig. 2.22** HRTEM image of a SiC nanotube structure with 3.8 Å spacing [Ref. 94]

had been grown were placed at positions marked B<sub>1</sub>–B<sub>4</sub>. The temperature of the system was set to 1,250°C for 40 min and B<sub>4</sub>–B<sub>1</sub> position temperatures were found to decrease from 980 to 850°C. Si nanowires were found in all B<sub>4</sub>–B<sub>1</sub> positions, but the quantities of Si nanowires decreased from B<sub>4</sub> to B<sub>1</sub>. However, at position B<sub>3</sub>, ~935°C, besides Si nanowires, multiwalled SiC nanotubes were also obtained. A typical image of the fabricated SiC nanotubes is shown in Fig. 2.22. The interlayer spacing of the SiC nanotubes ranges from 3.5 to 4.5 Å.

The SiC nanotubes are carbon-filled and open-ended, and use a high-temperature substitution reaction between multiwalled carbon nanotubes and Si powder. The mean diameter and diameter distribution (45–70 nm) are smaller than previously reported for SiC nanotubes [95].

Single-phase silicon carbide nanotubes were successfully synthesized by the reaction of carbon nanotubes with silicon powder at 1,200°C for 100 h [96]. TEM



observations revealed the formation of both single-phase SiC nanotubes and C–SiC coaxial nanotubes, which are carbon nanotubes sheathed with a SiC layer.

## 2.6 SiC Nanowire Heterostructures

1D nanowire heterostructures are important for their potential applications in nanodevices. There are three basic structures: axial heterostructures, in which the heterointerface is perpendicular to the wire axis, radial heterostructures, in which the heterointerface is parallel to the wire axis, and branched nanowire structures, in which the structures have branched and tree-like nanowire structures. Detailed information as to semiconductor nanowire heterostructures can be found in [97, 98].

Multielement nanotubes comprising multiple phases, with diameters of a few tens of nanometers and lengths up to 50  $\mu\text{m}$ , were successfully synthesized by means of reactive laser ablation in NEC Corporation [99]. A mixed and compressed powder of BN, C, SiO, and  $\text{Li}_3\text{N}$  acted as starting material. The synthesized structure consists of  $\beta\text{-SiC-SiO}_2\text{-BN/C}$  nanocables, as shown in Fig. 2.23. They have high aspect ratios with lengths of several tens of micrometers and diameters of a few tens of nanometers, which is relatively homogeneous for each wire. The structure resembles a coaxial nanocable with a semiconductor–insulator–metal (semiconductor–insulator–semiconductor) geometry and suggests applications in nanoscale electronic devices that take advantage of this self-organization mechanism for multielement nanotube formation. Later, heterostructures of single-walled SiC nanotubes and nanorods were fabricated by solid–solid reaction between single-walled carbon nanotubes (SWCNTs) and Si/Ti [100].

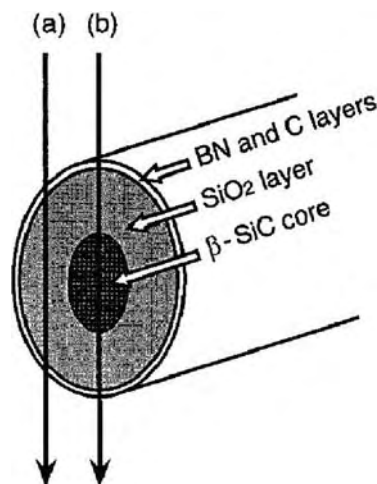


**Fig. 2.23** Multiphase nanocable. *Solid arrows* indicate the probe positions in the electron energy loss fine structure analysis (not shown) [Ref. 99]



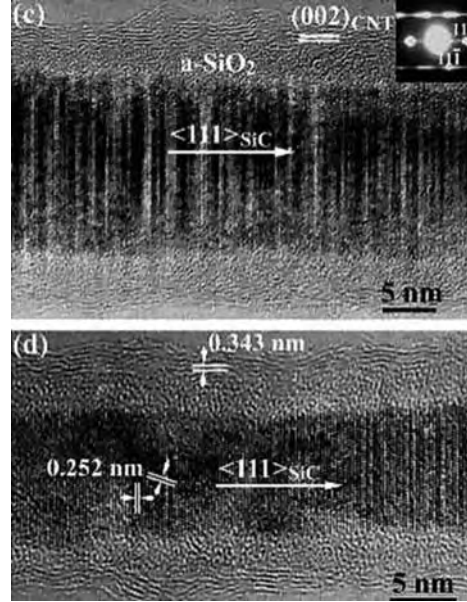
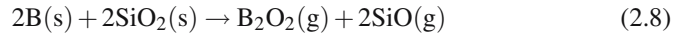


**Fig. 2.24** High-resolution TEM images of coaxial nanocables, displaying single-crystalline  $\beta$ -SiC cores, amorphous  $\text{SiO}_2$  intermediate layers (c), and outer graphitic C sheaths (d). The inset in (c) represents the corresponding ED pattern [Ref. 101]

Li et al. [101] reported a simple thermal evaporation route for the mass production of SiC– $\text{SiO}_2$ –CNT coaxial nanocables (Fig. 2.24). Most importantly, they found that these nanocables may be further transformed into nanochains of SiC–CNT junctions during high-temperature annealing at  $1,600^\circ\text{C}$  in a high vacuum of  $1.5 \times 10^{-3}$  Pa (Fig. 2.25).

An insulating tubular boron nitride (BN)-sheathed SiC semiconductor nanowire was synthesized [102–107]. The BN nanotube may serve as a naturally insulating and/or protective shield for any nanowire encapsulating within because of its advantages. Hexagonal BN, a covalently bonded compound, displays stable insulating properties ( $\sim 5.5$  eV bandgap) independent of its morphology. Moreover, graphitic-like BN is chemically inert and remarkably thermally stable [108].

The BN-sheathed SiC nanowires can be synthesized by heating a mixture of B and  $\text{SiO}_2$  with molar ratio of 1:1 [102]. The inside SiC nanowires exhibit a wide diameter distribution from several nanometers to 80 nm. The sheathed BN layer has a uniform coating thickness from 2 to 4 nm, which is independent of the diameter of the SiC nanowires.  $\text{B}_2\text{O}_3$  and SiO vapors were generated by heating the mixture of B and  $\text{SiO}_2$  powders at the high temperature of  $1,500^\circ\text{C}$  by the following solid-state reaction:



The simultaneously formed vapors ( $\text{B}_2\text{O}_3$  and SiO) were transported to a deposition area, where highly oriented pyrolytic graphite (HOPG) covered with fine nickel



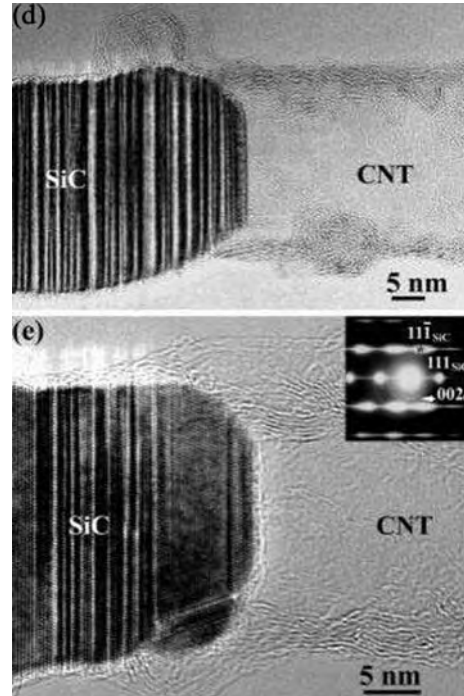


**Fig. 2.25** (d) and (e) selected high-resolution TEM images of SiC–CNT junctions after annealing [Ref. 101]

catalyst grains was placed. SiC and BN can be formed on the surface of HOPG in the presence of nitrogen by further reactions at about 1,400°C.



The ZnS/SiC nanocables and SiC-shelled ZnS nanoribbons were synthesized using ZnS nanowires and nanoribbons as templates via a controllable two-stage thermal process. First, ZnS nanowires were formed by heating SiO and ZnS powders. Then, the decomposition of CH<sub>4</sub> and disproportion of SiO resulted in the synthesis of SiC nanowires on the ZnS-based template surface [109].

A two-step process was used to synthesize a direct heterojunction of ZnO nanorods on SiC nanowires [110]. First, a nanowire substrate was synthesized by heating NiO-catalyzed Si wafer at 1,050°C. Then, diethylzinc was used as a metal-organic gas source to fabricate ZnO nanorods on SiC nanowires at 450°C. An atomically abrupt interface without interfacial layers was detected. ZrO<sub>2</sub> and metal coating on SiC nanowire were also synthesized by CVD [111–113].

The synthesis of SiC/ZnO shell–core nanostructures involved two steps [114]. First, ZnO nanostructures (nanobelt, nanocombs, nanojunctions, and nanohelices) were fabricated using a vapor–solid growth. Then, a SiC layer was deposited on



the surface of ZnO nanostructures via plasma-enhanced chemical vapor deposition (PECVD). The source materials for SiC were  $\text{CH}_4$  and  $\text{SiH}_4$  gases. Subsequent dissolution of ZnO (by HCl solution) left a SiC shell that preserved the same shape at the original ZnO nanostructure. This is one of the most effective methods for producing hollow nanostructures. The SiC shell nanostructures could have potential application in space-confined nanoreactors, catalysts, nanofluid channel, and drug delivery.

## 2.7 Properties of SiC Nanowires

### 2.7.1 Field Emission

Because of the small curvature of the tip radius, high ratio, chemical inertness, and electrical conductivity, SiC wide-bandgap semiconductors are considered to be promising for the next generation of large-area field-emission flat panel displays (FEDs) [115–119]. A series of experiments have been carried out to investigate the field-emission characteristics of the 1D SiC nanostructures, which indicate that the SiC nanowires are characteristic of excellent emitting behavior for application in field-emission technology.

The field-emission measurements were carried out in a vacuum chamber at a pressure of  $3 \times 10^{-5}$  Pa at room temperature. Figure 2.26 shows the schematic diagram of the field-emission experimental setup. A platinum film coated on glass substrate with SiC nanowires was used as a cathode and a stainless steel plate with a diameter of 6 mm was used as an anode. Before testing the field emission, a 0.008 g SiC sample (HF-etched SiC fabricated by the high-frequency heating invented by

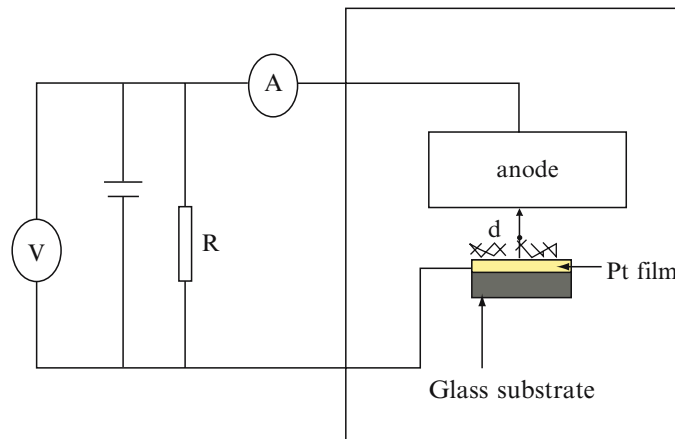


**Fig. 2.26** Experiment setup used for the field-emission measurement



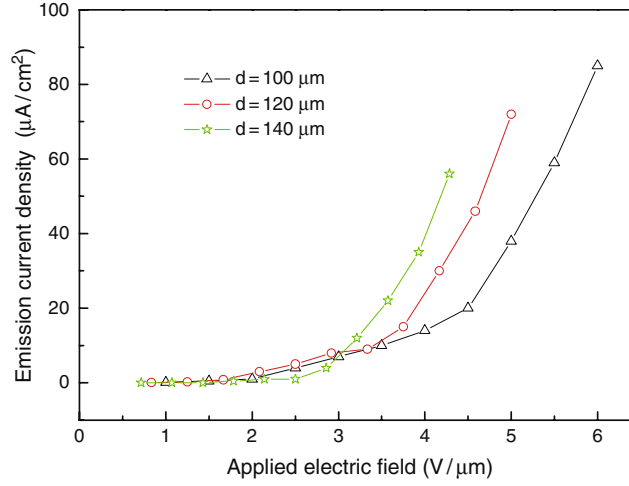


**Fig. 2.27** The dependence of the field-emission current density  $J$  on the applied electric field strength  $E$  of the samples at three anode-sample distances of 100, 120, and 140 μm

us) was sonicated into a suspension in deionized water (DE) for 20 min and 20 drops of DE solution of SiC were dropped on the platinum film and dried at 50°C. The distance ( $d$ ) between the emitting surface and the plate was determined by first lowering the plate to the product until electric contact was observed, then lifting the plate to a certain value [120]. Figure 2.27 shows the field-emission current density ( $J$ ) of the SiC nanowires as a function of the applied electric field ( $E$ ) at three anode-sample separation: 100, 120, and 140 μm. Here, we define the turn-on field as the electric field required to produce a current density of  $10 \mu\text{A cm}^{-2}$ . It can be seen that the turn-on field is dependent on the anode-sample distance, its value increase as the anode-sample distances decrease, and measured to be 3.5, 3.4, and  $3.1 \text{ V } \mu\text{m}^{-1}$ , respectively, which indicates the strong electron emission property of the SiC nanowires because of the high aspect ratio.

The field-emission property was also analyzed by applying the first-order approximation of Fowler–Nordheim (FN) theory to understand the emission characteristics, using the following equation [121]

$$J = 1.56 \times 10^{-6} E^2 / \Phi \exp(-6.83 \times 10^7 \Phi^{3/2} / E), \quad (2.11)$$

where  $J$  is the field-emission current density ( $\text{A cm}^{-2}$ ),  $\Phi$  is the work function of the emission tip (eV), and  $E$  is the microscopic local electric field at the emission sites ( $\text{V cm}^{-1}$ ). The actual value of  $E$  could not be measured directly and is related to the applied voltage  $V$  by setting  $E = \beta V / d$ , where  $d$  is the anode-sample separation and  $\beta$  is the field enhancement factor. The FN emission behavior can be examined from the linearity of curves plotting  $\ln(J/E^2)$  vs.  $1/E$  as shown in Fig. 2.28. It is found that they yield straight lines for the three different anode-sample distances in agreement with the Fowler–Nordheim equation, confirming that the current is indeed the



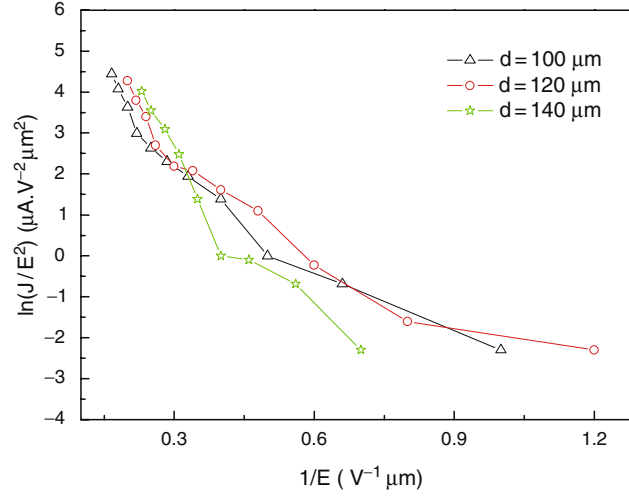


**Fig. 2.28** Fowler–Nordheim relationship of  $\ln(J/E^2) - 1/E$  plot at three anode-sample distances of 100, 120, and 140  $\mu m$

result of field emission. In other words, the field emission from SiC nanowires is a barrier tunneling, quantum mechanical process. Besides, the straight lines also show that the field emission is independent of the anode-sample separation, and only a function of the applied voltage. In addition, a stability and durability test was carried out on the SiC nanowires at anode-sample 100  $\mu m$  separation. The results show that field-emission current density of  $60 \mu A \text{ cm}^{-2}$  was recorded for 15 min at the same applied voltage of 550 V. The current fluctuation was as low as  $\pm 15\%$  and the average current did not decrease over this period.

The BN coatings reducing effectively the turn-on field of SiC nanowires were investigated by Tang [122]. It was found that BN–SiC 1D nanocomposite is a promising emitting material for applications in flat display. The low turn-on field is due to a decrease of the effective potential barrier height, which is considered to result from the existence of a defect-induced positive space charge. Figure 2.29 shows the field-emission plots for single-crystal  $\beta$ -SiC nanowires, BN nanotubes, and BN-coated SiC nanowires. The single-crystal SiC nanowires showed a high turn-on field at  $13 \text{ V } \mu m^{-1}$ . The turn-on field of pure BN nanotubes is also larger than  $14 \text{ V } \mu m^{-1}$ . But the pattern of field emission of BN–SiC nanowires clearly showed a low turn-on field at 6 and  $\sim 20 \text{ V } \mu m^{-1}$  of threshold field providing  $10 \text{ mA cm}^{-2}$  of current density, which is typically required for effectively exciting a phosphor pixel in flat display.

Core–shell SiC/SiO<sub>2</sub> nanowires were fabricated by directly heating Si substrate with Ni film under reductive environments using the carbothermal reduction of WO<sub>3</sub> by C [123]. The thickness of SiO<sub>2</sub> layer can be controlled by HF-etching duration. Figure 2.30 shows the field-emission currents from the bare SiC and the SiC/SiO<sub>2</sub> samples for various shell thickness. The turn-on field of the samples was  $4.0 \text{ V } \mu m^{-1}$



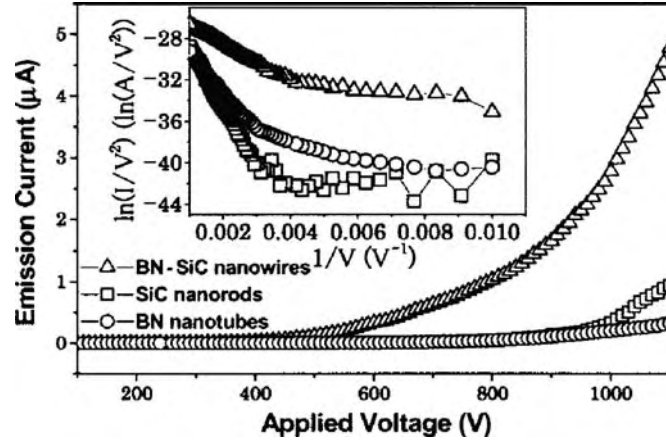


Fig. 2.29 Field-emission plots for single-crystal SiC nanowires, BN nanotubes, and BN-coated SiC nanowires. The insets show the corresponding FN plots [Ref. 122]

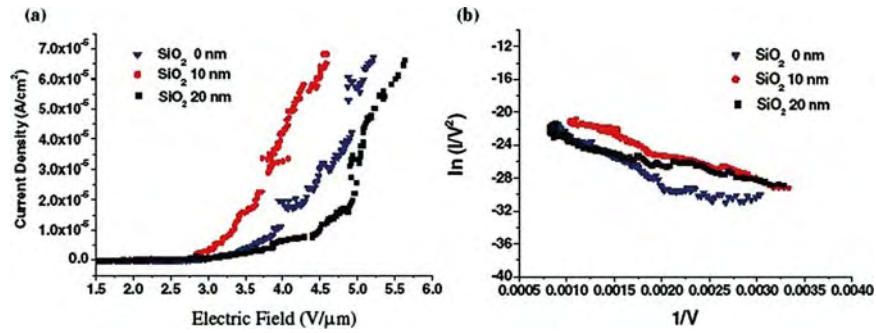


Fig. 2.30 (a) Current density ( $\text{A cm}^{-2}$ )–electric field ( $\text{V } \mu\text{m}^{-1}$ ) characteristics of core-shell SiC– $\text{SiO}_2$  and bare SiC nanowire emitters. (b) The Fowler–Nordheim plots of nanowires [Ref. 123]

(bare SiC nanowires),  $3.3 \text{ V } \mu\text{m}^{-1}$  (10 nm  $\text{SiO}_2$ -coated SiC), and  $4.5 \text{ V } \mu\text{m}^{-1}$  (20 nm  $\text{SiO}_2$ -coated SiC nanowires). It can be seen that SiC nanowires coated with an optimum  $\text{SiO}_2$  thickness (10 nm) have a higher field-emission current than bare SiC nanowires. It is because the wide-bandgap  $\text{SiO}_2$  shell layer has small electron affinity (0.6–0.8 eV) and can hence field emission properties of SiC nanowires. However, a very thick shell layer could induce charge buildup at the shell layer–SiC emitter due to limited electron supply through a thick insulating layer. The emission mechanism follows with Fowler–Nordheim equation.

The turn-on field of carbon-coated SiC nanowires at the emission current density of  $10 \text{ mA cm}^{-2}$  was about  $4.2 \text{ V } \mu\text{m}^{-1}$  [124]. The aligned SiC nanowires have a very low field ( $2.5\text{--}3.5 \text{ V } \mu\text{m}^{-1}$ ) to be excellent field emitter material.



### 2.7.2 Optical Properties

There have been some reports on the optical properties of SiC nanowires. Experiments showed that SiC nanowires have a significant redshift owing to the size confinement effect. Figure 2.31 shows the typical Raman spectra of SiC nanowires and SiC bulk ceramic target [71]. The SiC nanowires have the typical Raman features at  $\sim 784$  and  $938\text{ cm}^{-1}$  and both peaks have a marked redshift of 12 and  $34\text{ cm}^{-1}$  compared to the TO and LO phonon modes of bulk SiC.

SiC/SiO<sub>2</sub> nanocables were synthesized by the low-cost arc-discharge method in deionized water [125]. The SiC with 10 nm core diameter possesses two broad PL peaks at 317 and 368 nm (Fig. 2.32a). But two emission peaks of the SiC nanowires with 20 nm diameter are located at 312 and 393 nm. It is believed that the second peak results from the central  $\beta$ -SiC nanowire and the blueshift may be the result of the quantum size effects. The thinner the central SiC nanorod is, the higher the correspondent PL peak energy is.

The PL spectra of the SiC with core diameter of 20 nm are shown in Fig. 2.32b. It can be seen that the positions of the PL peaks change little while the strength changed significantly. It can also be noted that high-temperature annealing would release the local stress formed during the growth of the nanocables and decrease the amount of defects; then the PL peak's intensity and position would change.

The  $\beta$ -SiC nanowires with different diameters, synthesized by our high-frequency heating method, were investigated by Fourier transition infrared (FT-IR) spectroscopy. In the FT-IR spectrum, each curve has strong adsorption peaks (Fig. 2.33). The values of  $781$  and  $1,045\text{ cm}^{-1}$ ,  $788$  and  $1,082\text{ cm}^{-1}$ , and  $800$  and

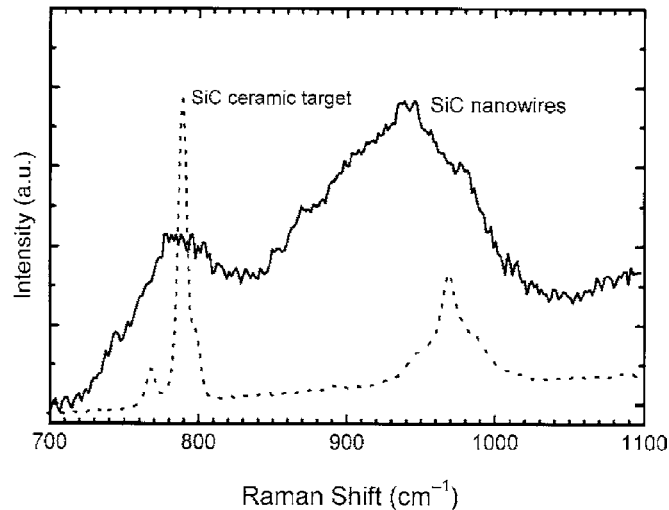


**Fig. 2.31** Raman spectrum of SiC nanowires by laser ablation



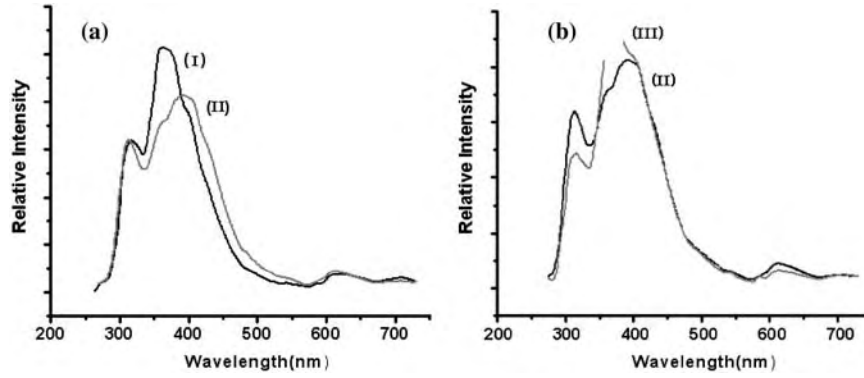


Fig. 2.32 (a) PL spectra of the as-prepared SiC nanocables with core diameters of 10 nm (I) and 20 nm (II), respectively. (b) The PL spectra of the SiC nanocables with core diameter of 20 nm before (II) and after (III) annealing

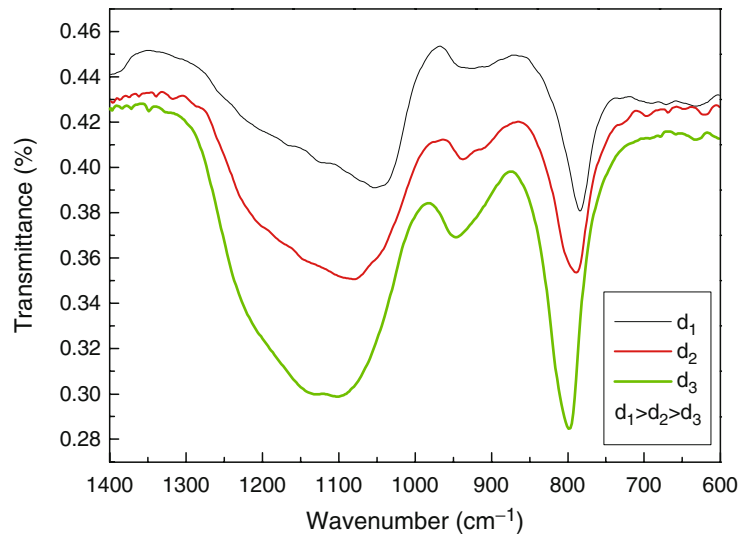


Fig. 2.33 IR spectrum of  $\beta$ -SiC nanowires with different diameters.  $d_i$  is the diameter of SiC

$1,100\text{cm}^{-1}$  are for SiC nanowires with different mean diameters, namely 36.9, 24.8, and 15.5 nm, respectively. The first value of each curve is the characteristic peak of SiC, and the second value is attributed to  $\text{SiO}_2$ . Compared with  $760\text{cm}^{-1}$  of bulk SiC and  $1,040\text{cm}^{-1}$  of  $\text{SiO}_2$ , the different SiC nanowires have a significant bulk-shift, and the bulk-shift value number increased with the decreased diameter of SiC nanowires.



### 2.7.3 Electron Transport Properties

#### 2.7.3.1 Electrical Transport in Individual SiC

Li [126] synthesized SiC nanowires with BN sheaths by high-temperature evaporation of a mixture of Si and  $\text{In}_2\text{O}_3$  powders in a small BN crucible at  $1,600^\circ\text{C}$  for 1 h. The electrical transport of the individual SiC/BN nanowires was measured by AFM. It showed that the BN nanotube sheath is a good insulation layer between the SiC nanowire core and Au electrode (contacting points 1 and 2). Point 3 coated by gold and the  $I$ - $V$  curve confirm good conductivity. The bare SiC nanowire had a high semiconductor behavior (Fig. 2.34). Hence, the construction of complex 3D networks made from the present nanostructures becomes possible with the independent electrical performance of each 1D nanostructure.

#### 2.7.3.2 SiC Nanowire Field-Effect Transistors

The SiC nanowire field-effect transistor was investigated systematically by Zhou et al. [127]. The electronic measurement configuration for a bottom-contacted nanowire device following drop deposition of a single nanowire onto prepatterned

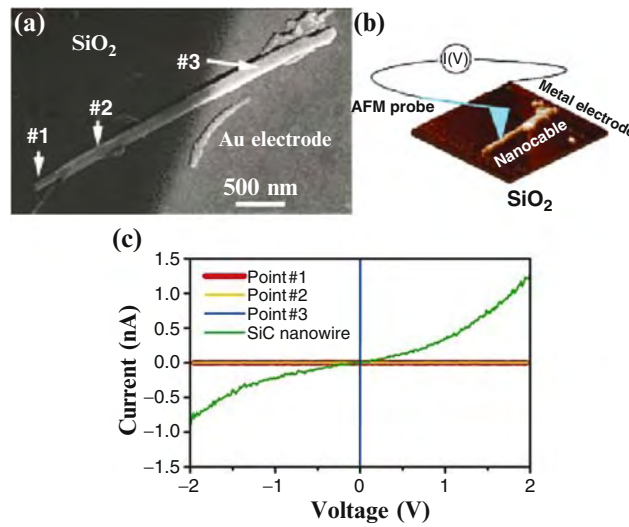


**Fig. 2.34** (a) SEM image of a BN-SiC nanocable partially covered on the right by a metal electrode. The left tip end of its SiC core protrudes from the BN sheath whereas the right tip is encapsulated in it. The three designated points were used for electrical contacting with an AFM tip. (b) 3D AFM image of the nanocable and schematic of the two-probe measurement with the AFM tip. (c)  $I$ - $V$  curves taken at contacting points 1–3, and on a bare SiC nanowire. No current was detected for the SiC-BN nanocable within the sensitivity of the experimental setup ( $\sim 2$  pA), whereas SiC nanowires without any coating exhibited semiconducting behavior [Ref. 126]



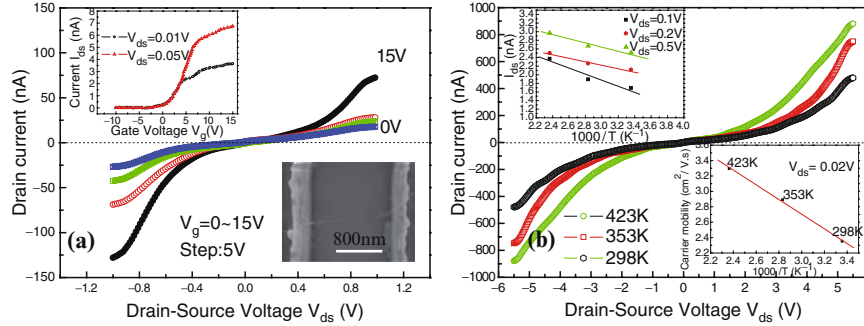


**Fig. 2.35** (a) Current ( $I_{ds}$ ) vs. voltage ( $V_{ds}$ ) curves recorded for different gate voltages at room temperature. *Low-right inset*: the SiC nanowire bridges the two electrodes. *Left inset*: typical  $I_{ds}$  vs.  $V_g$  curves measured at a drain voltage of 0.01 and 0.05 V, respectively. (b)  $I_{ds} - V_{ds}$  curves obtained at the different temperatures at  $V_g = 5$  V. *Low-right inset*: Arrhenius plots of mobility of SiC FET for various temperature. *Left inset*: temperature dependence of  $I_{ds}$  of the SiC nanowire FET with Au contact electrodes at  $V_g = 5$  V

gold microelectrodes on oxidized Si chip substrates (Fig. 2.35a (low-right inset)) shows a SEM image of a typical device, where a nanowire can be seen bridging two gold electrodes. A typical  $I_{ds} - V_{ds}$  characteristic of SiC FETs is shown in Fig. 2.35a. It is very clear that the conductance increased monotonically with the increase of the gate voltage  $V_g$ , which corresponds to n-type properties of the SiC nanowire channel.

From Fig. 2.35a (left inset) and the formula [128]

$$\mu_e = g_m L^2 / C V_{ds}, \quad (2.12)$$

where transconductance ( $g_m$ ) is expressed as  $g_m = dI_{ds}/dV_g$  and  $C$  is the gate capacitance estimated by

$$C = 2\pi\epsilon\epsilon_0 L / \ln(2h/r), \quad (2.13)$$

where  $\epsilon$ ,  $h$ , and  $r$  are the dielectric constant, the thickness of silicon dioxide, and the radius of the SiC nanowire, respectively. It can be obtained as  $\mu_e = 15.9$  and  $6.4 \text{ cm}^2 \text{ V}^{-1} \text{ s}^{-1}$  from the formula for  $V_{ds} = 0.01$  and  $0.05$  V, respectively. The transconductance ( $g_m$ ) that is obtained from the linear portion of the curve has the value of  $10 \times 10^{-10}$  and  $5 \times 10^{-10} \text{ A V}^{-1}$  at  $V_{ds} = 0.05$  and  $0.01$  V, respectively (Fig. 2.35a, left inset). The normalized transconductance of  $5 \times 10^{-10}$  and  $2.5 \times 10^{-10} \text{ A V}^{-1} \text{ m}^{-1}$ , respectively. In addition, the transistor has an on-off ratio of nearly  $10^3$ . The carrier concentration of SiC FET is approximately  $0.82 \times 10^7$  and  $1.76 \times 10^7 \text{ cm}^{-1}$  at  $V_{ds} = 0.01$  and  $0.05$  V, respectively. Compared with the theoretical value of the bulk  $\beta$ -SiC ( $\sim 1,000 \text{ cm}^2 \text{ V}^{-1} \text{ s}^{-1}$ ), the results are very low for 1D nanoscale confinement and scattering from the lattice defects and electron-electron interaction.

Figure 2.35b shows the temperature dependence of the drain current of the n-type SiC nanowire FET at  $V_g = 5$  V. It can be seen that the drain current increased



by one order of magnitude at high temperature from that at room temperature. It is commonly believed that the role of the  $V_g$  is to change the value of  $R_{\text{SiC}}$  through Fermi level (EF) modulation, thus changing the slope. Figure 2.35b (low-right inset) shows the carrier mobility in log scale as a function of  $1,000/T$  at  $V_{\text{ds}} = 0.02 \text{ V}$ . The liner relation, as observed in the figure, suggests an Arrhenius function

$$\mu_e = \mu_0 \exp(-E_a/kT), \quad (2.14)$$

where  $E_a$  is the activation energy,  $\mu_0$  is the preexponential factor, and  $k$  is the Boltzmann constant. The carrier mobility increased with the increasing temperature and has an activated energy of 82 meV.

The dependence of the  $I_{\text{ds}}$  in log scale on  $1,000/T$  at  $V_g = 5 \text{ V}$  and  $V_{\text{ds}} = 0.1, 0.2$ , and  $0.5 \text{ V}$  is shown in the left inset of Fig. 2.35b. The results tally with the thermionic emission of carriers, in which the current  $I \propto \exp(-\Phi_b/kT)[\exp(qV_{\text{ds}}/kT)]^{-1}$ , the barrier heights between the Au electrodes and SiC nanowire were extracted from the slope as  $\Phi_b = 58.5, 39.3$ , and  $39.6 \text{ meV}$  for  $V_{\text{ds}} = 0.1, 0.2$ , and  $0.5 \text{ V}$ , respectively.

#### 2.7.4 Mechanical Properties

1D nanostructures are supposed to be significantly stronger than their counterparts. Wong [129] used atomic force microscopy to determine the mechanical properties of individual, structurally isolated SiC NRs that were pinned at one end to molybdenum disulfide surfaces. The bending force was measured against displacement along the unpinned lengths. The strengths of the SiC nanorods were substantially greater (610–660 GPa) than those found previously for larger SiC structures, and they approach theoretical values. These results are in good agreement with the 600 GPa value predicted theoretically for [111] oriented SiC, the average values obtained previously for micrometer diameter whiskers.

Wang et al. [130, 131] used another method called the resonance vibration for measuring the mechanical properties of the SiC nanowire. The experimental results are in agreement with theoretically expected values. Some measured and theoretical values are shown in Tables 2.3 and 2.4.

**Table 2.3** Measured Young's modulus for core-shell SiC/SiO<sub>2</sub> nanowire

$D_s$ (nm) ( $\pm 2 \text{ nm}$ )	$D_c$ (nm) ( $\pm 1 \text{ nm}$ )	$L$ ( $\mu\text{m}$ ) ( $\pm 0.2 \mu\text{m}$ )	$f_0$ (MHz)	$E_{\text{eff}}$ (GPa) Exp.	$E_{\text{eff}}$ (GPa) Theor.
51	12.5	6.8	0.693	$46 \pm 9.0$	73
74	26	7.3	0.953	$56 \pm 9.2$	78
83	33	7.2	1.044	$52 \pm 8.2$	82
132	48	13.5	0.588	$78 \pm 7.0$	79
190	105	19.0	0.419	$81 \pm 5.1$	109

$D_s$  and  $D_c$  are the outer and inner of the SiO<sub>x</sub> sheath, respectively.  $L$  the nanowire length,  $f_0$  the fundamental resonance frequency



**Table 2.4** Measured Young's modulus of biaxially structured SiC–SiO<sub>x</sub> nanowires

$D_{\text{wire}}$ (nm) ( $\pm 2$ nm)	$D_{\text{SiC}}$ (nm) ( $\pm 1$ nm)	$L$ ( $\mu\text{m}$ ) ( $\pm 0.2 \mu\text{m}$ )	$f_0$ (MHz)	$E_{\text{eff}}$ (GPa) Exp.
58	24	4.3	1.833	$54 \pm 24.1$
70	36	7.9	0.629	$53 \pm 8.4$
83	41	4.3	2.707	$61 \pm 13.8$
92	47	5.7	1.750	$64 \pm 14.3$

$D_{\text{wire}}$  and  $D_{\text{SiC}}$  are the widths across the entire nanowire and across the SiC subnanowire, respectively

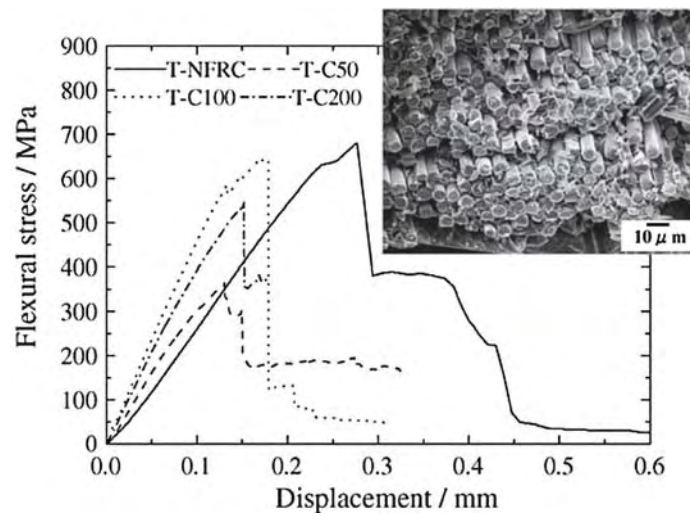


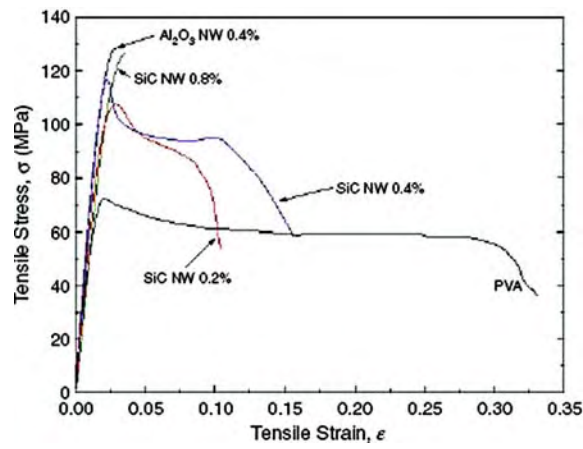
**Fig. 2.36** Typical flexural stress–displacement curves and fiber pullout fracture surface (T-NFRC) [Ref. 133]

The measured values of SiC nanowires suggest that SiC nanowires can be used as reinforcement materials for ceramic matrix composites to improve their strength and toughness. Fabrication and flexural properties (measured by three-point bending) of a SiC nanowire/Tyranno-SA fiber-reinforced SiC/SiC composite made by the chemical vapor infiltration (CVI) process have been reported [132–134]. A representative flexural stress–displacement curve is shown in Fig. 2.36. The composite T-NFRC (T stands for Tyranno-SA fiber and NFRC stands for SiC nanowire/fiber-reinforced composites) possesses common features with conventional Tyranno-SA/SiC composites upon flexural fracture. However, the SiC nanowire-reinforced Tyranno-SA/SiC composites show marked improvements on the flexural strength and work of fracture compared with a series of conventional Tyranno-SA/SiC composites (T-C50, T-C100, and T-C200). The flexural properties, such as flexural modulus ( $E_f$ ), proportional limit stress (PLS), ultimate flexural strength ( $\sigma_u$ ), and the fracture energies ( $W_f$ ), are give in Table 2.5.



**Table 2.5** Density, interlayer, and flexural properties of composite with SiC nanowires and conventional composites

Composite ID	Density ( $\text{mg m}^{-3}$ )	Pyc layer (nm)	$E_f$ (GPa)	PLS (MPa)	$\sigma_u$	$W_f$
T-NFRC	$2.62 \pm 0.03$	60	$120 \pm 17$	$570 \pm 120$	$660 \pm 77$	$6.1 \pm 0.7$
T-C50	$2.41 \pm 0.03$	50	$140 \pm 13$	$260 \pm 5$	$410 \pm 92$	$1.8 \pm 0.5$
T-C100	$2.63 \pm 0.04$	100	$160 \pm 11$	$430 \pm 32$	$610 \pm 28$	$3.2 \pm 0.4$
T-C200	$2.61 \pm 0.03$	200	$140 \pm 10$	$340 \pm 18$	$550 \pm 58$	$2.3 \pm 0.3$

**Fig. 2.37** Tensile stress–strain curves of PVA and NW composites, showing an increase in the ultimate tensile strength and reduction in ductility with increasing NW volume fraction [Ref. 135]

Rao et al. [135] have investigated the mechanical properties of composites of SiC nanowire-reinforced polymer–matrix (PVA) composites. Experimental results show that enhancements of these mechanical properties occur even with a small vol% addition of SiCNWs. A representative curve of tensile stress vs. strain is shown in Fig. 2.37. With increasing SiC nanowire volume fraction ( $V_f$ ), a significant increase in the yield strength takes place. PVA without SiC nanowire reinforcement behaves like an elastic, perfectly plastic solid. The 0.8 vol% SiCNW composites show near-zero ductility, fracturing immediately after yielding. The composites exhibit higher strength; a significant strain softening is seen immediately after the peak in the load. Figure 2.38 shows tensile strength as a function of nanowire volume fraction. As for the SiC nanowire-reinforced composite, the strength of the composites increases markedly initially and reaches a plateau. The initial hardening rate is commensurate with the strength of the SiCNWs. The measured result is compatible with the least-square fit of the equation.



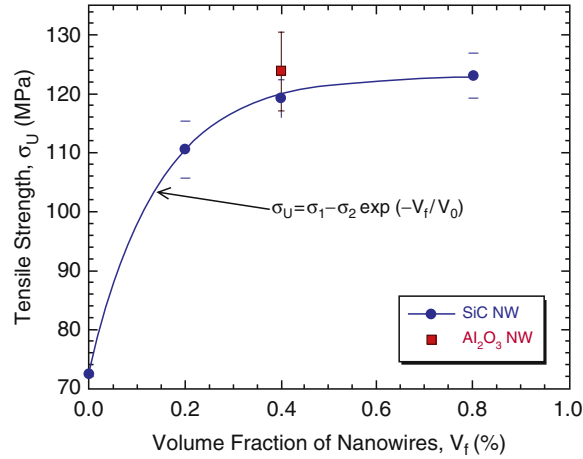


**Fig. 2.38** Variation of tensile strength as function of nanowire volume fraction. The *solid line* represents the least-square fit to the equation given in the figure [Ref. 135]

### 2.7.5 Photocatalyst Properties

The photocatalytic activity of the SiC nanowires was evaluated by measuring the photodegradation rates of  $CH_3CHO$  for SiC in a quartz vessel as a function of UV irradiation time under UV light ( $1.5 \text{ mW cm}^{-2}$ ) [136]. It was found from Fig. 2.39a that the increase of the initial gaseous acetaldehyde concentration leads to a strengthened conversion of gaseous acetaldehyde. This is attributed to the larger amount of gaseous acetaldehyde molecules attached to the surface of the SiC nanowire powders. After 6 h, the photodegradation of SiC to the initial 100 ppm of gaseous acetaldehyde is 54.99%, increased by 12% for the initial 50 ppm of gaseous acetaldehyde. These results, shown in Fig. 2.39b, are also corroborated by the concentration variation of produced  $CO_2$ , evolved as result of photodecomposition of acetaldehyde, as a function of irradiation time. The  $CO_2$  concentration increases with the photodegradation rate of gaseous acetaldehyde. That is to say, the acetaldehyde is converted into  $CO_2$ . Besides, the synthesized SiC nanowires coated with  $SiO_2$  layers have higher photocatalytic activity than the HF-treated (bare) SiC nanowires. Semiconducting SiC nanowires offer an alternative to titanium and other metal oxides for use in smart nanoelectronics for environmental control and monitoring, which is highlighted by *Nature Nanotechnology* [137].

### 2.7.6 Hydrogen Storage Properties

Since the time it was proved that carbon nanotubes (CNTs) can store hydrogen [59], several experimental and theoretical attempts have been performed to investigate



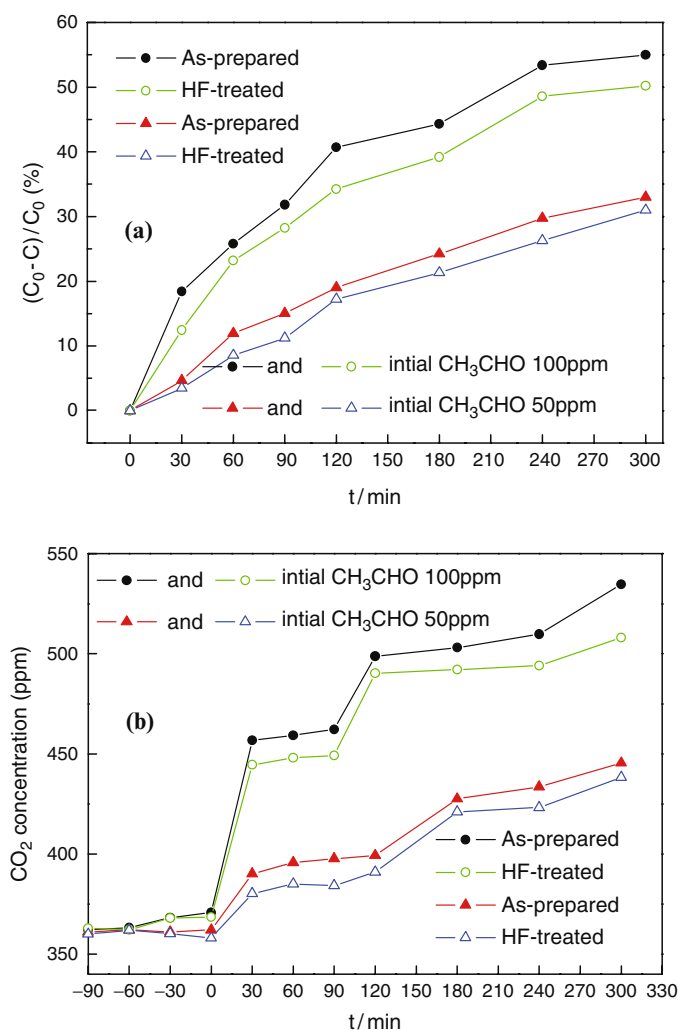


**Fig. 2.39** (a) SiC photodegradation rates as a function of irradiation time during the photodegradation of acetaldehyde gas under UV irradiation and (b) CO<sub>2</sub> evolution as a function of irradiation time (light on at zero) during the photodegradation of acetaldehyde gas under UV irradiation

hydrogen adsorption in CNTs. A detailed review of inorganic nanotubes can be found [138–140]. In the case of SiC nanotubes that store hydrogen, no record of the experiment is available. However, theoretical work is underway. Recently, Mpourmpakis and Froudakis [141] reported hydrogen storage in SiCNTs by a multiscale theoretical approach. First, *ab initio* calculations at the density functional level of theory (DFT) showed an increase of 20% in the binding energy of H<sub>2</sub> in SiCNTs compared with pure CNTs. Second, classical Monte Carlo simulation of nan-



otube bundles showed an even larger increase of the storage capacity in SiCNTs, especially in low-temperature and high-pressure conditions. Both the results indicate that SiCNTs seem to be more suitable materials for hydrogen storage than pure CNTs.

## 2.8 Concluding Remarks

This chapter has reviewed the synthesis of SiC 1D nanostructures (nanowire/nanotube) and their applications. The unique properties of SiC nanowires and nanotubes make them good candidates for nanodevices and nanocomposites. From the published literature on 1D SiC nanostructures, it can easily be seen that research on 1D SiC nanostructures mainly focuses on synthesis methods. Optical properties (PL and Raman spectra, etc.) are also reported. However, theoretical research on the mechanical properties, electronic properties, and quantum confinement effect of  $\beta$ -SiC is scarcely reported [142–146]. Hence, intensive work would be attempted to investigate various properties of 1D SiC nanowires on the experimental and theoretical levels. An understanding of the mechanical, electronic, transport, thermal, and other properties would be gained, as well as the fundamental physical phenomenon of 1D SiC nanostructures differing from bulk SiC.

In the next stage, some issues should be highlighted. (1) SiC nanostructure materials fabricated previously were in the shape of hollow nanosphere, nanosprings, nanoflower, and nanotubes. However, some novel synthesized methods of SiC nanostructures are still being developed. Various kinds of 1D SiC nanostructures would be fabricated in high yields at low cost, for example, SiC with other semiconductors in the form of core-shell and hybrid heteronanostructures. The diameter, position, and length, of nanostructures can easily be controlled. Besides, the growth kinetics and thermodynamics of 1D SiC nanostructures are complex, and fully understanding them will help to device/modulate the desired rich morphologies of 1D SiC nanowires. (2) The doping for semiconductor materials applicable to 1D SiC nanostructure materials is a hot topic, because the optical, magnetic, electrical, and electrochemical properties of as-doped SiC can be modified on a nanometer scale. (3) SiC nanowires/nanotubes could be promising candidates to act as connections at nanoscale because they have exceptional mechanical, electronic, and optical properties. Most importantly, self-assembling nanocircuits made from SiC nanowire/nanotube building blocks may play an important role in future nanodevices for next-generation electronic devices. (4) It may be possible to develop a novel SiC nanowire synthesized process compatible with the state-of-the-art Si semiconductor technology. (5) The SiC-reinforced matrix composites are expected to find an application in aerospace and the flexible electronic field. (6) SiC nanowires are ideally suited as interfaces capable of efficiently bridging biological systems and nanoelectronic devices because of their biocompatibility [143]. The explorations of the fundamental properties of SiC have found that it can enrich applications in nanodevices (sensor, detector, and actuator) nanocomposites and biological systems.



**Acknowledgements** This work is jointly supported by Shanghai Municipal Commission for Science and Technology (Grant No. 03DZ14025), Developing Foundation of Shanghai Science and Technology Grant No. 0452nm056 and National Basic Research Program of China No 2006CB300406 and 2007CB935400, China Postdoctoral Scientific Foundation founded project (20070420105). The authors are grateful to all the other authors of related papers and some cited Figures.

## References

1. Liu W, Lieber CM (2006) Semiconductor nanowires. *J. Phys. D: Appl. Phys.* 39:R387–R406
2. Thelander C, Agarwal P (2006) Nanowire-based one-dimensional electronics. *Mater. Today* 9:28–35
3. Rao CNR, Deepak FL, Gundiah G, Govindaraj A (2003) Inorganic nanowires. *Progr. Solid State Chem.* 31:5–147
4. Wang ZL (2003) *Nanowires and Nanobelts*. Kluwer, New York
5. Li Y, Qian F, Xiang J, Lieber CM (2006) Nanowire electronic and optoelectronic devices. *Mater. Today* 9:18–27
6. Zhang DH, Wang YY (2006) Synthesis and applications of one-dimensional nano-structured polyaniline: An overview. *Mater. Sci. Eng. B* 134:9–19
7. Samuelson L, Thelander C, Björk MT, Borgström, M (2004) Semiconductor nanowires for 0D and 1D physics and applications. *Physica E* 25:313–318
8. <http://www.lib.demokritos.gr/InTheNews/emerging0204.htm>
9. Buttner CC, Zacharias M (2006) Retarded oxidation of Si nanowires. *Appl. Phys. Lett.* 89:263106.1–263106.3
10. Wang N, Tang YH, Zhang YF, Lee CS, Lee ST (1998) Nucleation and growth of Si nanowires from silicon oxide. *Phys. Rev. B* 58:R16024–R16026
11. Hasunuma R, Komeda T, Mukaida H, Tokumoto H (1997) Formation of Si nanowire by atomic manipulation with a high temperature scanning tunneling microscope. *J. Vac. Sci. Technol. B* 15:1437–1441
12. Rougemaille N, Schmid AK (2006) Self-organization and magnetic domain microstructure of Fe nanowire arrays. *J. Appl. Phys.* 99:08S502–08S504
13. Oon CH, Khong SH, Boothroyd CB, Thong JT (2006) Characteristics of single metallic nanowire growth via a field-emission induced process. *J. Appl. Phys.* 99:064309–064320
14. Wu Y, Xiang J, Yang C, Lu W, Lieber CM (2004) Single-crystal metallic nanowires and metal/semiconductor nanowire heterostructures. *Nature* 430:61–65
15. Cha SN, Jang JE, Choi Y (2006) High performance ZnO nanowire field effect transistor using self-aligned nanogap gate electrodes. *Appl. Phys. Lett.* 89:63102–63104
16. Sanghyun J, Kangho L, Janes DB (2005) Low operating voltage single ZnO nanowire field-effect transistors enabled by self-assembled organic gate nanodielectrics. *Nano Lett.* 5:2281–2286
17. Wang X, Sun XY (2006) Fabrication of GaN nanowire arrays by confined epitaxy. *Appl. Phys. Lett.* 89:233115–233117
18. Motayed A, He MQ (2006) Realization of reliable GaN nanowire transistors utilizing dielectrophoretic alignment technique. *J. Appl. Phys.* 100:114310–114318
19. Yin LW, Bando Y, Zhu YC (2004) Synthesis of InN/InP core/sheath nanowires. *Appl. Phys. Lett.* 84:1546–1548
20. Heo YW, Norton DP, Tien LC, Kwon Y, Kang BS, Ren F, Pearton SJ, LaRoche JR (2004) ZnO nanowire growth and devices. *Mater. Sci. Eng.: R Rep.* 47:1–47
21. Ren S, Bai YF, Chen J (2007) Catalyst-free synthesis of ZnO nanowire arrays on zinc substrate by low temperature thermal oxidation. *Mater. Lett.* 61:666–670
22. Liang C, Towe E, Kuball M (2006) Opto-electronic simulation of GaN nanowire lasers GaN, AlN, InN and related materials. *Mater. Res. Soc. Symp. Proc.* 892:225–230



23. Magdas DA, Cremades A (2006) Three dimensional nanowire networks and complex nanostructures of indium oxide. *J. Appl. Phys.* 100:094320–094324
24. Vaddiraju S, Mohite A, Chin A (2005) Mechanisms of 1D crystal growth in reactive vapor transport: Indium nitride nanowires. *Nano Lett.* 5:1625–1631
25. Tao T, Song H, Wu J (2004) Synthesis and characterization of single-crystal indium nitride nanowires. *J. Mater. Res.* 19:423–426
26. Chang CY, Chi GC, Wang WM (2006) Electrical transport properties of single GaN and InN nanowires. *J. Electron. Mater.* 35:738–743
27. Yang J, Liu TW, Hsu CW (2006) Controlled growth of aluminium nitride nanorod arrays via chemical vapour deposition. *Nanotechnology* 17:S321–S326
28. Li ZJ, Shen ZQ, Wang Fu (2006) Arc-discharge synthesis and microstructure characterization of AlN nanowires. *J. Mater. Sci. Technol.* 22:113–116
29. Mingo N (2003) Calculation of Si nanowire thermal conductivity using complete phonon dispersion relations. *Phys. Rev. B* 68:113308–113310
30. Wang N, Zhang YF, Tang YH, Lee CS, Lee ST (1998) SiO<sub>2</sub>-enhanced synthesis of Si nanowires by laser ablation. *Appl. Phys. Lett.* 73:3902–3904
31. Wang ZY, Hu J, Yu MF (2006) One-dimensional ferroelectric monodomain formation in single crystalline BaTiO<sub>3</sub> nanowire. *Appl. Phys. Lett.* 89:263119–263121
32. Park JM, Kim SJ, Kim PG, Yoon DJ, Hansen G, DeVries KL (2007) Self-sensing and actuation of CNF and Ni nanowire/polymer composites using electro-micromechanical test. *Proc. SPIE* 6463:64630–64634
33. Salfi J, Philipose U, deSousa CF, Aouba S, Ruda HE (2006) Electrical properties of Ohmic contacts to ZnSe nanowires and their application to nanowire-based photodetection. *Appl. Phys. Lett.* 89:261112–261114
34. Tutuc E, Chu JO, Ott JA, Guha S (2006) Doping of germanium nanowires grown in presence of PH<sub>3</sub>. *Appl. Phys. Lett.* 89:263101–263103
35. Chen YJ, Chen XD, Li BJ, Yu DS, He ZQ, Li GJ, Zhang MQ (2006) Optical properties of synthesized organic nanowires. *Appl. Phys. Lett.* 89:241121–241123
36. Feng P, Zhang JY, Li QH, Wang TH (2006) Individual-Ga<sub>2</sub>O<sub>3</sub> nanowires as solar-blind photodetectors. *Appl. Phys. Lett.* 88:153107–153109
37. He MQ, Mohammad SN (2006) Novel chemical-vapor deposition technique for the synthesis of high-quality single-crystal nanowires and nanotubes. *J. Chem. Phys.* 124:064714–064720
38. Xiang J, Lu W, Hu YJ, Wu Y, Yan H, Lieber CM (2006) Ge/Si nanowire heterostructures as high-performance field-effect transistors. *Nature* 441:489–493
39. Zhong ZH, Wang DL, Cui Y, Bockrath MW, Lieber CM (2003) Nanowire Crossbar arrays as address decoders for integrated nanosystems. *Science* 302:1377–1379
40. Cui Y, Wei QQ, Park HK, Lieber CM (2001) Nanowire nanosensors for highly sensitive and selective detection of biological and chemical species. *Science* 293:1289–1292
41. Huber CA, Huber TE, Sadoqi M, Lubin JA, Manalis S, Prater CB (1994) Nanowire array composites. *Science* 263:800–802
42. Huang MH, Mao S, Feick H, Yan HQ, Wu YY, Kind H, Weber E, Russo R, Yang PD (2001) Room-temperature ultraviolet nanowire nanolasers. *Science* 292:1897–1899
43. Hong BH, Bae SC, Lee CW, Jeong SM, Kim KS (2001) Ultrathin single-crystalline silver nanowire arrays formed in an ambient solution phase. *Science* 294:348–351
44. Wang ZL, Song JH (2006) Piezoelectric nanogenerators based on zinc oxide nanowire arrays. *Science* 312:242–246
45. Ruff M, Mittlehner H, Helbig R (1994) SiC devices: Physics and numerical simulation. *IEEE Trans. Electron. Devices* 41:1040–1054
46. Morkoc H, Strite S, Gao GB, Lin ME, Sverdlov B, Burns M (1994) Large-band-gap SiC, III–V nitride, and II–VI ZnSe-based semiconductor device technologies. *J. Appl. Phys.* 76:1363–1398
47. Cicero G, Catellani A, Galli G (2004) Atomic control of water interaction with biocompatible surfaces: The case of SiC(001). *Phys. Rev. Lett.* 93:016102–016105
48. Harris GL (1995) *Properties of Silicon Carbide*. INSPEC, the Institution of Electrical Engineers, London



49. Zetterling CM (2002) *Process Technology for Silicon Carbide Devices*. EMIS Processing Series, no. 2. INSPEC, IEE, UK
50. Casady JB, Johnson RW (1996) States of silicon carbide (SiC) as a wide-bandgap semiconductor for high-temperature applications: A review. *Solid State Electron.* 39:1409–1422
51. Baliga BJ (1996) *Power Semiconductor Devices*. PWS-Kent, Boston, MA
52. Treu M, Rupp R, Blaschitz P (2006) Commercial SiC device processing: Status and requirements with respect to SiC based power devices. *Superlattice Microstruct.* 40:380–387
53. Sha JJ, Park JS, Hinoki T, Kohyama A (2007) Bend stress relaxation of advanced SiC-based fibers and its prediction to tensile creep. *Mech. Mater.* 39:175–182
54. Mehregany M, Zorman CA (1999) SiC MEMS: Opportunities and challenges for applications in harsh environments. *Thin Solid Films* 355–356:518–524
55. Djenkal D, Goeuriot D, Thevenot F (2000) SiC-reinforcement of an  $\text{Al}_2\text{O}_3$ - $\gamma$  AlON composite. *J. Eur. Ceram. Soc.* 20:2585–2590
56. Müller G, Krötz G, Niemann E (1994) SiC for sensors and high-temperature electronics. *Sens. Actuators A: Phys.* 43:259–268
57. Dimitrijević S, Jamet P (2003) Advances in SiC power MOSFET technology. *Microelectron. Reliab.* 43:225–233
58. Iijima S (1993) Helical microtubules of graphitic carbon. *Nature* 354:56–58
59. Iijima S, Ichihashi T (1993) Single-shell carbon nanotubes of 1-nm diameter. *Nature* 363:603–605
60. Zhou D, Seraphin S (1994) Production of silicon carbide whiskers from carbon nanoclusters. *Chem. Phys. Lett.* 222:233–238
61. Dai HJ, Wong EW, Lu YZ, Fan SS, Lieber CM (1995) Synthesis and characterization of carbide nanorods. *Nature* 375:769–772
62. Han WQ, Fan SS, Li QQ, Liang WJ, Gu BL, Yu DP (1997) Continuous synthesis and characterization of silicon carbide nanorods. *Chem. Phys. Lett.* 265:374–378
63. Tang CC, Fan SS, Dang HY, Zhao JH, Zhang C, Li P, Gu A (2000) Growth of SiC nanorods prepared by carbon nanotubes-confined reaction. *J. Cryst. Growth* 210:595–599
64. Muñoz E, Dalton AB, Collins S, Zakhidov AA (2002) Synthesis of SiC nanorods from sheets of single-walled carbon nanotubes. *Chem. Phys. Lett.* 395:397–402
65. Seeger T, Redlich PK, Rühle M (2000) Synthesis of nanometer-sized SiC whiskers in the arc-discharge. *Adv. Mater.* 12:279–282
66. Li YB, Xie SS, Zou XP, Tang DS, Liu ZQ, Zhou WY, Wang G (2001) Large-scale synthesis of  $\beta$ -SiC nanorods in the arc-discharge. *J. Cryst. Growth* 223:125–128
67. Thess A, Lee R, Nikolaev P, Dai H, Petit P (1996) Crystalline ropes of metallic carbon nanotubes. *Science* 273:483–487
68. Liu J, Rinzler AG, Dai H, Hafner JH, Bradley PK, Boul PJ, Lu A (1998) Fullerene pipes. *Science* 280:1253–1255
69. Zhang YF, Tang YH, Wang N, Yu DP, Lee CS, Bello I, Lee ST (1998) Silicon nanowires prepared by laser ablation at high temperature. *Appl. Phys. Lett.* 72:1835–1837
70. Tang YH, Zhang YF, Peng HY, Wang N, Lee CS, Lee ST (1999) Si nanowires synthesized by laser ablation of mixed SiC and  $\text{SiO}_2$  powders. *Chem. Phys. Lett.* 314:16–20
71. Shi WS, Zheng YF, Peng HY, Wang N, Lee CS, Lee ST (2000) Laser Ablation synthesis and optical characterization of silicon carbide nanowires. *J. Am. Ceram. Soc.* 83:3228–3230
72. Meng GW, Cui Z, Zhang LD, Phillipp F (2000) Growth and characterization of nanostructured  $\beta$ -SiC via carbothermal reduction of  $\text{SiO}_2$  xerogels containing carbon nanoparticles. *J. Cryst. Growth* 209:801–806
73. Liang CH, Meng GW, Zhang LD, Wu YC, Cui Z (2000) Large-scale synthesis of  $\beta$ -SiC nanowires by using mesoporous silica embedded with Fe nanoparticles. *Chem. Phys. Lett.* 329:323–328
74. Xu WJ, Xu Y, Sun XY, Liu YQ, Wu D, Sun YH (2006) Fabrication of tower like  $\beta$ -like by sol-gel and carbothermal reduction processing. *New Carbon Mater.* 21:167–170
75. Yang W, Araki H, Thaveethavorn S, Suzuki H, Nada T (2005) In situ synthesis and characterization of pure SiC nanowires on silicon wafer. *Appl. Surf. Sci.* 241:236–240



76. Yang W, Araki H, Hu QL, Ishikawa N, Suzuki S, Noda T (2004) In situ growth of SiC nanowires on RS-SiC substrates. *J. Cryst. Growth* 264:278–283
77. Ying YC, Gu Y, Li ZF, Gu HZ, Cheng LY, Qia YT (2004) A simple route to nanocrystalline silicon carbide. *J. Solid State Chem.* 177:4163–4166
78. Mamails AG, Vogtlander LOG, Markopoulos A (2004) Nanotechnology and nanostructured materials: Trends in carbon nanotubes. *Precis. Eng.* 28:16–30
79. Zhang YF, Gamo MN, Xiao CY, Ando T (2002) Synthesis of 3C-SiC nanowhiskers and emission of visible photoluminescence. *J. Appl. Phys.* 91:6066–6070
80. Zhou XT, Wang N, Lai HL, Peng Y, Bello I, Lee ST (1999)  $\beta$ -SiC nanorods synthesized by hot filament chemical vapor deposition. *Appl. Phys. Lett.* 74:3942–3944
81. Chio HJ, Seong HK, Lee JC, Sung YM (2004) Growth and modulation of silicon carbide nanowires. *J. Cryst. Growth* 269:472–478
82. Ho GW, Wong SW, Kang DJ, Welland ME (2004) Three-dimensional crystalline SiC nanowire flowers. *Nanotechnology* 15:996–999
83. Li HJ, Li ZJ, Meng AL, Li KZ, Zhang XN, Xu YP (2003) SiC nanowire networks. *J. Alloys Compd.* 352:279–282
84. Zhang YJ, Wang NL, He RR, Chen XH, Zhu J (2001) Synthesis of SiC nanorods using floating catalyst. *Solid State Commun.* 118:595–598
85. Zhou WM, Yang B, Yang ZX, Zhu F, Yan LJ, Zhang YF (2006) Large-scale synthesis and characterization of SiC nanowires by high-frequency induction heating. *Appl. Surf. Sci.* 252:5143–5148
86. Zhou WM, Yang ZX, Zhu F, Zhang YF (2006) SiC/SiO<sub>2</sub> nanocables and nanosprings synthesized by catalyst-free method. *Physica E* 31:9–12
87. Zhang HF, Wang CM, Wang SL (2002) Helical crystalline SiC/SiO<sub>2</sub> core-shell nanowires. *Nano Lett.* 2:941–944
88. Kong XY, Wang ZL (2003) Spontaneous polarization-induced nanohelices, nanosprings, and nanorings of piezoelectric nanobelts. *Nano Lett.* 3:1625–1631
89. Shen GZ, Bando YS, Ye CH, Liu BD, Golberg D (2006) Synthesis, characterization and field-emission properties of bamboo-like  $\beta$ -SiC nanowires. *Nanotechnology* 17:3468–3472
90. Shen GZ, Bando YS, Golberg D (2006) Self-assembled hierarchical single-crystalline  $\beta$ -SiC nanoarchitectures. *Crystal growth & design* 7:35–38
91. Li ZJ, Zhang JL, Meng A, Guo JZ (2006) Large-area highly oriented SiC nanowires: Synthesis, Raman, and photoluminescence properties. *J. Phys. Chem. B* 110:22382–22386
92. Pan ZW, Lai HL, Au CK, Duan XF, Zhou WY, Shi WS, Wang N, Lee CS, Wong NB, Lee ST, Xie SS (2000) Oriented silicon carbide nanowires: Synthesis and emission properties. *Adv. Mater.* 12:1186–1190
93. Kim HY, Park J, Yang H (2003) Direct synthesis and aligned silicon carbide nanowires from the silicon substrates. *Chem. Commun.* 37:256–257
94. Sun XH, Li CP, Wong WK, Wong NB, Lee CS, Lee ST, Teo BK (2002) Formation of silicon carbide nanotubes and nanowires via reaction of silicon (from disproportionation of silicon monoxide) with carbon nanotubes. *J. Am. Chem. Soc.* 124:14464–14472
95. Palen EB, Ruemmeli MH, Gemming T, Knupfer M, Biedermann K, Leonhardt A, Pichler T (2005) Bulk synthesis of carbon-filled silicon carbide nanotubes with a narrow diameter distribution. *J. Appl. Phys.* 97:056102–056104
96. Taguchi T, Igawa N, Yamamoto H (2004) Synthesis of silicon carbide nanotubes. *J. Am. Ceram. Soc.* 88:459–461
97. Lauhon LJ, Gudiksen MS, Lieber CM (2004) Semiconductor nanowire heterostructures. *Philos. Trans. R. Soc. Lond. A* 362:1247–1260
98. Lu W, Lieber CM (2006) Semiconductor nanowires. *J. Phys. D: Appl. Phys.* 39:R387–R406
99. Zhang Y, Suenage K, Colliex C, Iijima S (1998) Coaxial nanocable: Silicon carbide and silicon oxide sheathed with boron nitride and carbon. *Science* 281:973–975
100. Zhang Y, Ichihashi T, Landree E, Nihey F, Iijima S (1999) Heterostructures of single-walled carbon nanotubes and carbide nanorods. *Science* 285:1719–1722
101. Li YB, Bando YS, Golberg D (2004) SiC-SiO<sub>2</sub>-C coaxial nanocables and chains of carbon nanotube-SiC heterojunctions. *Adv. Mater.* 16:93–96



102. Tang CC, Bando YS, Sato TD, Kurashima KJ (2002) Uniform boron nitride coatings on silicon carbide nanowires. *Adv. Mater.* 14:1406–1409
103. Han WQ, Redlich P, Ernst F, Ruhle M (1999) Synthesizing boron nitride nanotubes filled with SiC nanowires by using carbon nanotubes as templates. *J. Appl. Lett.* 75:1875–1877
104. Tang CC, Bando YS, Sato TD, Kurashima KJ (2002) SiC and its bicrystalline nanowires with uniform BN coatings. *Appl. Phys. Lett.* 80:4641–4643
105. Wenger KS, Cornu D, Chassagneux F, Ferro G, Epicier T, Miele P (2002) Direct synthesis of  $\beta$ -SiC and h-BN coated  $\beta$ -SiC nanowires. *Solid State Commun.* 124:157–161
106. Tang CC, Bando YS, Sato TD, Kurashima KJ (2002) Comparative studies on BN-coating on SiC and  $\text{Si}_3\text{N}_4$  nanowires. *J. Mater. Chem.* 12:1910–1913
107. Pokropivny V, Pokropivny A, Lohmus A, Lohmus R, Kovrygin S, Sylenko P, Partch R, Prilutskii E (2006) Extremely high-frequency piezoelectroacoustic transducer based on BN-tube/SiC-whiskers rope. *Physica E* 37:283–286
108. Zhu YC, Bando YS, Xue DF, Xu FF, Golberg D (2003) Insulating tubular BN sheathing on semiconducting nanowires. *J. Am. Chem. Soc.* 125:14226–14227
109. Hu JQ, Bando Y, Zhan JH, Golberg D (2004) Fabrication of ZnS/SiC nanocables, SiC-shelled ZnS nanoribbons (and sheets), and SiC nanotubes (and tubes). *Appl. Phys. Lett.* 85:2932–2934
110. Tak YJ, Ryu YH, Yong KJ (2005) Atomically abrupt heteronanojunction of ZnO nanorods on SiC nanowires prepared by a two-step. *Nanotechnology* 16:1712–1716
111. Tak YG, Yong KJ (2005)  $\text{ZrO}_2$ -coated SiC nanowires prepared by plasma-enhanced atomic layer chemical vapor deposition. *Surf. Rev. Lett.* 12:215–219
112. Lalonde AD, Norton MG, McIlroy DN, Zhang DQ (2005) Metal coatings on SiC nanowires by plasma-enhanced chemical vapor deposition. *J. Mater. Res.* 20:549–553
113. Min BD, Lee JS, Cho KG, Hwang JW, Kim H, Sung MY, Kim S, Park J, Seo HW, Bae SY, Lee MS, Park SO, Moon JT (2003) Semiconductor nanowires surrounded by cylindrical  $\text{Al}_2\text{O}_3$  shells. *J. Electron. Mater.* 32:1344–1348
114. Zhou J, Liu J, Yang R, Lao CS, Gao PX, Tummala R, Xu NS, Wang ZL (2006) SiC-shell nanostructures fabricated by replicating ZnO nano-objects: A technique for producing hollow nanostructures of desired shape. *Small* 2:1344–1347
115. Wu ZS, Deng SZ, Xu NS, Chen J, Zhou J, Chen J (2002) Needle-shaped silicon carbide nanowires: Synthesis and field electron emission properties. *80:3829–3831*
116. Wong KW, Zhou XT, Au CK, Lai HL, Lee CS, Lee ST (1999) Field-emission characteristics of SiC nanowires prepared by chemical-vapor deposition. *Appl. Phys. Lett.* 75:2918–2920
117. Lo HC, Hwang JS, Chen KH, Hsu CH, Chen CF, Chen LC (2003) SiC-capped nanotip arrays for field emission with ultralow turn-on field. *Appl. Phys. Lett.* 83:1420–1422
118. Feng DH, Jia TQ, Li XX, Xu ZZ, Chen J, Deng SZ (2003) Catalytic synthesis and photoluminescence of needle-shaped 3C-SiC nanowires. *Solid State Commun.* 128:295–297
119. Deng SZ, Li ZB, Wang WL, Xu NS, Zhou J, Zheng XG, Xu HT, Chen J, She JC (2006) Field emission study of SiC nanowires/nanorods directly grown on SiC ceramic surface. *Appl. Phys. Lett.* 89:023118–023200
120. Zhou WM, Wu YJ, Kong ESW, Zhu F, Hou ZY, Zhang YF (2006) Field emission from nonaligned SiC nanowires. *Appl. Surf. Sci.* 253:2056–2058
121. Fowler RH, Nordheim LW (1928) Electron beams formed by photoelectric field emission. *Proc. R. Soc. Lond. A* 119:173–181
122. Tang CC, Bando Y (2003) Effect of BN coatings on oxidation resistance and field emission of SiC nanowires. *Appl. Phys. Lett.* 83:659–661
123. Ryu YW, Tak YJ, Yong KJ (2005) Direct growth of core-shell SiC-SiO<sub>2</sub> nanowires and field emission characteristics. *Nanotechnology* 16:S370–S374
124. Ryu YH, Park BT, Song YH, Yong K (2004) Carbon-coated SiC nanowires: Direct synthesis from Si and field emission characteristics. *J. Cryst. Growth* 271:99–104
125. Liu XM, Yao KF (2005) Large-scale synthesis and photoluminescence properties of SiC/SiO<sub>x</sub> nanocables. *Nanotechnology* 16:2932–2935
126. Li YB, Dorozhkin PS, Bando YS, Golberg D (2005) Controllable modification of SiC nanowires encapsulated in BN nanotubes. *Adv. Mater.* 17:545–549



127. Zhou WM, Fang F, Hou ZY, Yan LJ, Zhang YF (2006) Field-effect transistor based on  $\beta$ -SiC nanowire. *IEEE Electron. Device Lett.* 27:463–465
128. Avouris P, Martel R, Derycke V, Appenzeller J (2002) Carbon nanotube transistors and logic circuits. *Phys. B* 323:6–14
129. Wong EW, Sheehan PE, Lieber CM (1997) Nanobeam mechanics: Elasticity, strength, and toughness of nanorods and nanotubes. *Nature* 277:1971–1975
130. Wang ZL, Dai ZR, Gao RP, Bai ZG, Gole JL (2000) Side-by-side silicon carbide–silica biaxial nanowires: Synthesis, structure, and mechanical properties. *Appl. Phys. Lett.* 77: 3349–3351
131. Wang ZL, Dai ZR, Gao RP, Bai ZG, Gole JL (2002) Measuring the Young's modulus of solid nanowires by in situ TEM. *J. Electron. Microsc.* 51(Suppl.):S79–S85
132. Yang W, Araki H, Kohyama A, Katoh Y, Hu Q, Suzuki H, Noda T (2004) Tyranno-SA/SiC composite with SiC nanowires in the matrix by CVI process. *J. Nucl. Mater.* 329–333: 539–543
133. Yang W, Araki H, Kohyama A, Thaveethavorn S, Suzuki H, Noda T (2004) Fabrication in-situ SiC nanowires/SiC matrix composite by chemical vapour infiltration process. *Mater. Lett.* 58:3145–3148
134. Yang W, Araki H, Tang CC, Thaveethavorn S, Kohyama A, Suzuki H, Noda T (2005) Single-crystal SiC nanowires with a thin carbon coating for stronger and tougher ceramic composites. *Adv. Mater.* 17:1519–1523
135. Vivekchand SRC, Ramamurty U, Rao CNR (2006) Mechanical properties of inorganic nanowire reinforced polymer–matrix composites. *Nanotechnology* 17:S344–S350
136. Zhou WM, Yan LJ, Wang Y, Zhang YF (2006) SiC nanowires: A photocatalytic nanomaterial. *Appl. Phys. Lett.* 89:013105–013107
137. <http://www.nature.com/nnano/reshigh/2006/0706/full/nnano.2006.21.html>
138. Remškar M (2004) Inorganic nanotubes. *Adv. Mater.* 16:1497–1504
139. Tenne R, Rao CNR (2004) Inorganic nanotubes. *Philos. Trans. R. Soc. Lond. A* 362:2099–2125
140. Ma RZ, Golberg D, Bando YS, Sasaki T (2004) *Philos. Trans. R. Soc. Lond. A* 362:2161–2186
141. Mpourmpakis G, Froudakis GE (2006) SiC nanotubes: A novel material for hydrogen storage. *Nano Lett.* 6:1851–1853
142. Yan BH, Zhou G, Duan WH, Wu J, Gu BL (2006) Uniaxial-stress effects on electronic properties of silicon carbide nanowires. *Appl. Phys. Lett.* 89:023104–023106
143. Rurali R (2005) Electronic and structural properties of silicon carbide nanowire. *Phys. Rev. Lett.* 71:205405.1–205405.7
144. Kim TY, Han SS, Lee HM (2004) Nanomechanical behavior of  $\beta$ -SiC nanowire in tension: Molecular dynamic simulations. *Mater. Trans.* 45:1442–1449
145. Moon WH, Ham JK, Hwang HJ (2003) Mechanical properties of SiC nanotubes. *Technical Proceedings of the 2003 Nanotechnology Conference and Trade Show*, vol. 3, pp 158–161
146. Cicero G, Catellani A, Galli G (2004) Atomic control of water interaction with biocompatible surfaces: The case of SiC(001). *Phys. Rev. Lett.* 93:016102.1–016102.4





<http://www.springer.com/978-0-387-74131-4>

One-Dimensional Nanostructures

Wang, Z.M. (Ed.)

2008, XII, 330 p., Hardcover

ISBN: 978-0-387-74131-4